Updating the Fast Grain Boundary program: Temperature-time paths from intragrain oxygen isotope zoning

Gabriel Kropf[a,1], Chloë Bonamici[b,2], Brian Borchers[a]

[a]Department of Mathematics, New Mexico Tech, Socorro, USA

[b]Department of Geoscience, University of Wisconsin-Madison, Madison, USA

Highlights:

- Fast Grain Boundary program (Eiler et al. 1994) re-written in Python and C
- Addition of a graphical user interface
- Ability to invert oxygen isotope zoning profiles for T–t paths
- Tests for functionality and sensitivity with synthetic and real oxygen isotope data

Link to code: https://github.com/gkropf/FastGrainBoundary-DiffusionSolver

Authorship statement: Kropf wrote the FGB code in Python and C, including additions for the GUI and inversion functions, produced several synthetic tests and initial inversion results for real data, and wrote the first version of the manuscript. Bonamici co-supervised research and performed condensation and revision of the manuscript. Borchers co-supervised research and generated or revised some synthetic data tests.

[1] Present address: Coalition Inc.; gabriel@coalitioninc.com
[2] Corresponding author; bonamici@wisc.edu; Lewis G. Weeks Hall, 1215 W. Dayton St., Madison, WI 53706

ABSTRACT

This contribution presents a rewritten and expanded version of the Fast Grain Boundary (FGB) program (Eiler et al. 1994) with the motivation of adding to the geochemical tools available for reconstructing temperature-time (*T*–*t*) histories that inform studies of tectonics and crustal evolution. Both the original and the new FGB programs model the oxygen-isotope compositional evolution of a rock resulting from diffusive oxygen isotope exchange between minerals. The new FGB program is coded in Python and includes a graphical user interface. Additionally, C-compiled versions of the code are available that provide a 20x speedup of model calculations. The new implementation also allows for inversion of the FGB model to extract unbiased thermal histories from oxygen isotope data. The Levenberg-Marquardt (LM) algorithm is applied to search for cooling histories that maximize agreement between the model output and the measured oxygen isotope data. Tests with synthetic datasets show that the LM algorithm is able to distinguish between simple linear cooling and more complex thermal histories that include reheating events. Inversion of a natural oxygen isotope zoning dataset from titanite shows that, within the resolution of the models and data, the Adirondack Mountains sample location experienced rapid (30-70 °C/m.y.), monotonic cooling from 700 to 500 °C. We develop a heuristic guide to sampling and analytical approaches that improve the resolution of inversion solutions for current SIMS analytical capabilities and suggest targets for future improvements of SIMS analysis. Our tests indicate that the current SIMS analytical precision for in situ oxygen isotope measurements is sufficient to allow for temperature-time path recovery with thermal resolution of 25-50 °C and temporal resolution of 2-3 million years.

Keywords: Fast Grain Boundary; temperature-time path; oxygen isotopes; inversion thermal history

1. INTRODUCTION

Magmatic and tectonic events produce distinctive temperature variations in the crust (e.g., England and Thompson, 1984). Recognizing past magmatic or tectonic events, especially in regions with significant erosion, poor exposure, or protracted and complicated geologic histories, often hinges on recognizing their thermal effects in the rock record. Many minerals gain or lose constituents by mass diffusion in response to changing temperature. Some minerals can therefore reflect crustal thermal history in the spatial pattern of elements or isotopes that results from thermally activated diffusive mass redistribution. Providing that these spatial patterns – i.e., elemental or isotopic zoning – can be recognized and measured within a mineral (or minerals), they will represent a time-integrated record of the thermal conditions experienced by the minerals' host rock. Recognizing and measuring diffusion-induced intragrain zoning are non-trivial tasks (e.g., Eiler et al., 1995; Bindeman et al., 2008; Watts et al., 2012; Stearns et al., 2015; Rubin et al., 2017), as is deconvolving the thermal history that such zoning represents (e.g., Eiler et al., 1995; Storm and Spear, 2005; Smye and Stockli, 2014; Watson and Cherniak, 2015).

Oxygen, the most abundant element in Earth, has three isotopes (^{16}O, ^{17}O, and ^{18}O) that partition between minerals based on temperature and bulk rock composition (e.g., Urey, 1947; Chacko et al. 2001). The $^{18}O/^{16}O$ ratio – $\delta^{18}O$, when normalized to a standard of

known $^{18}O/^{16}O$ – of coexisting minerals and fluids have long been used to uniquely constrain rock crystallization temperature, assuming that the phases in question reached isotopic equilibrium (e.g., Urey, 1948; Jenkin et al. 1994; Valley, 2001; Holder et al. 2018). More recently, geochemists have exploited the time dependence of diffusive oxygen isotope exchange between phases to constrain the rates of temperature change in rocks (e.g., Farver, 1989; Jenkin et al., 1991; Eiler et al. 1992). It is now possible to measure $\delta^{18}O$ in many minerals with high precision and high spatial resolution by secondary ion mass spectrometry (SIMS) (e.g., Valley and Kita, 2009; Kita et al. 2010), providing a means to detect $\delta^{18}O$ variations produced by thermally activated diffusion.

In this contribution, we describe a numerical implementation of the Fast Grain Boundary (FGB) model (Eiler et al., 1993, 1992), which can be used to interpret rock thermal histories from oxygen isotope zoning preserved within one or more minerals of a rock sample (Fig. 1). The new FGB implementation has been updated and expanded from the original version developed by Eiler et al. (1994) and reported in this journal more than 25 years ago. The FGB model describes the closed-system, diffusive exchange of oxygen isotopes between minerals within a rock in response to temperature variations and the oxygen isotopic zoning that develops within each mineral as a result of the exchange. The reincarnation of the FGB program can be used either to fit a thermal history to measured oxygen isotope data through forward modeling or can perform statistically rigorous inversion of measured oxygen isotope data to back out a range of possible thermal histories.

The new FGB implementation described here shares similarities with at least four other well-known and widely used numerical thermochronology modeling tools – the multi-diffusion domain (MDD) model of Lovera et al. (1997, 2002) and Harrison et al. (2005), HeFTy of Ketcham (2005), and QtqT of Gallagher (2012), as well as with an iterative Markov Chain Monte Carlo modeling approach developed by Smye et al. (2018). FGB is, however, distinct from HeFTy, QtqT, MDD, and the MCMC of Smye et al. (2018) in a few important ways. First and foremost, whereas existing models describe primarily diffusion of trace elements (e.g., Ar, He, Pb), FGB describes the diffusive exchange of isotopes of oxygen, a major element in all silicate and oxide minerals on Earth. Models of trace element diffusion, first by Dodson (1986, 1973) and then by many subsequent workers (e.g., Cherniak, 1993; Smye and Stockli, 2014; Warren et al., 2012), employ a constant, zero-concentration grain boundary condition to simulate loss of the diffusant to an essentially infinite-sink reservoir outside the grain. To first order, this is an appropriate model for diffusion of structurally insignificant trace elements in many minerals, but it is not realistic for the case of major-element diffusion, in which a large fraction of the total mass of the system is diffusing. Major-element diffusion is only possible if mass balance is maintained within a closed system, such that oxygen lost from one mineral is taken in by another mineral. In FGB, this mass balanced oxygen isotope exchange occurs in response to, and is modulated by, an evolving grain boundary condition (non-zero, temperature-dependent, and time-dependent).

Another unique characteristic of FGB arising from the need to maintain mass balance is that FGB models a rock system, rather than a single phase within a rock. Primary user inputs to build a model are the mineral phases present, the mineral modes, the mineral grain sizes, and a whole-rock $\delta^{18}O$ value. The exchange equilibria and kinetics are

defined through oxygen isotope equilibrium fractionation factors (as a function of temperature) and oxygen diffusivity parameters for all phases. An equilibrium or near-equilibrium fluid phase may be modeled implicitly as part of the rock system by user selection of "wet" diffusivity parameters for mineral phases. The FGB model outputs are also holistic in the sense that the program either predicts diffusive oxygen isotope zoning for every mineral phase in the rock system (Fig. 2), or it can simultaneously invert the measured oxygen isotope zoning in multiple phases to constrain the thermal history.

FGB further differs from existing models in that it has the potential to constrain a continuous thermal history over a wide range of temperatures, including in the high temperature range (~500-800 °C). Oxygen diffusivity is different in every mineral phase and thus each mineral will transition from rapid to very slow (unmeasurable) oxygen diffusion over a different temperature range, analogous to the thermochronology concept of the partial retention zone or PRZ (e.g., Wolf et al., 1998). Diffusive oxygen isotope zoning in a given mineral thus provides a continuous thermal history over the mineral's particular PRZ. If oxygen isotope zoning develops in several minerals with overlapping PRZs – a realistic scenario in a multi-phase rock and, in fact, required for intragrain oxygen isotope exchange (Eiler et al., 1992) – then inversion of the zoning in all phases can constrain a continuous time-temperature history that extends from the PRZ of the mineral with the lowest oxygen diffusivity down through the PRZ of the mineral with the highest oxygen diffusivity. For comparison, MDD can also constrain a continuous thermal history but over a limited temperature range between ~400-150 °C, depending on the exact domain-size distribution in a given K-feldspar grain or grains (e.g., Harrison et al., 2005). HeFTy and QtQT models can be used to constrain thermal histories over a large range of temperatures, but much of this range, and especially the higher temperature part of the range, is constrained by a few, discrete *T*–*t* points provided by thermochronometers like U-Pb in monazite (e.g., Kirkland et al., 2017).

Finally, FGB differs from HeFTy, QtqT, and MDD in that it is a geospeedometry tool that provides information about durations and rates of thermal events but is not intrinsically linked to absolute geologic time. Because oxygen isotopes are stable, their abundances do no vary as a function of time through radioactive decay. In order to anchor the thermally induced diffusion of oxygen to a date, the minerals in which oxygen isotope zoning is recorded must be related through careful textural analysis to minerals that act as geochronometers. In many rocks, at least one mineral can be utilized both for oxygen isotope geospeedometery and for geochronometry – e.g., K-feldspar or titanite – providing a close link between the thermal history and absolute dates.

This contribution describes updates to the FGB code and its approach to thermal history inversion from oxygen isotope zoning data. We detail two examples of synthetic thermal histories and their recovery through inversion, as well as one example from a small natural data set. We also use FGB to explore how the choice of rock sample and analytical improvements could increase the resolution of thermal histories retrieved from inversion.

2. THEORY/METHOD

2.1 The Fast Grain Boundary Model & Its Forward Implementation

2.1.1 The Fast Grain Boundary conceptual model

The Fast Grain Boundary model describes the diffusive exchange of oxygen between multiple phases within a rock volume. Oxygen isotope exchange is driven by a system's

attempt to reach thermodynamic equilibrium, but it is achieved through specific mechanisms and at a finite rate and is thus governed by kinetics. The underlying behavior is modeled by Fick's first and second laws of mass diffusion, which relate diffusant flux and temporal variations in diffusant concentration, respectively, to spatial gradients in diffusant concentration (e.g., Crank, 1975).

The FGB model is based on the idea that oxygen diffusion through mineral structures is slow compared to oxygen diffusion along mineral grain boundaries (Fig. 3). Thus, grain boundaries achieve and maintain isotopic equilibrium, but grain interiors may not. Oxygen-isotope zoning may develop within a mineral grain in response to the variations in the equilibrium $\delta^{18}O$ concentration that is imposed at a grain's boundary (Fig. 3). Diffusion of oxygen through a mineral structure governs oxygen flux and flux rate into or out of a particular phase, whereas equilibrium isotope partitioning determines how the isotopes of oxygen are distributed (via grain boundaries) amongst phases. The closed system mass balance requirement of the system translates to a flux balance imposed at the mineral grain boundaries: at any given time, the total amount of oxygen lost to the grain boundary region by diffusion must equal the total amount of diffusive oxygen uptake into mineral grains. The balance imposed at the grain boundary between oxygen flux and oxygen isotope partitioning allows construction of a matrix of equations that couples volume diffusion through multiple phases to time-varying equilibrium conditions.

2.1.2 The updated Fast Grain Boundary numerical model

The numerical implementation of the FGB forward model, as laid out originally by Eiler et al. (1994) and updated by Bonamici (2013), are briefly reviewed here and in more detail in the Supplemental Materials. Figure 4 shows relations between the physical rock system and model equations. Diffusive exchange of oxygen between mineral phases in the model rock is driven by temperature variations, which are imposed through finite time steps and the time-temperature relationship, $T(t)$, set by the user. At each time step, the temperature is updated through the $T(t)$ function, as are the temperature-dependent equilibrium fractionations, $\Delta_{i\text{-}j}(T)$, and diffusivity, $D(T)$, for each mineral (Fig. 4). Oxygen diffusivities for each mineral are calculated by the Arrhenius relation. The program then solves for concentration profiles (c_i, concentration as a function of distance from core to rim of a mineral grain) in each mineral using a one-dimensional Crank-Nicholson finite difference scheme with spherical or cylindrical diffusion geometry and a grain boundary $\delta^{18}O$ fixed at the equilibrium $\delta^{18}O$ value determined in the previous time step. Spatial steps in the finite difference grid in each mineral are ~0.5-20 μm. Time steps are small compared to the total model run duration (typically in the range 1,000 – 10,000 yrs) and satisfy the Fourier stability criterion. The $\delta^{18}O$ flux is calculated for a given time step for a given mineral with a discretized version of Fick's first law. Mass balance is then imposed on the system by requiring that all fluxes from all minerals sum to zero for a given time step. The equilibrium fractionation equations provide m-1 constraints for calculating the equilibrium oxygen isotope concentrations for a set of m minerals at a given temperature. The final m^{th} constraint is provided by the mass flux balance. Then all fractionation and flux equations are solved simultaneously for updated equilibrium grain boundary $\delta^{18}O$ values:

$$\begin{bmatrix} 1 & -1 & 0 & \dots & 0 \\ 1 & 0 & -1 & \dots & 0 \\ \vdots & & & & \vdots \\ 1 & & & & -1 \\ k_1 & k_2 & \dots & \dots & k_m \end{bmatrix} \begin{bmatrix} c_{1,n}^{(k+1)} \\ c_{2,n}^{(k+1)} \\ \vdots \\ c_{m-1,n}^{(k+1)} \\ c_{m,n}^{(k+1)} \end{bmatrix} = \begin{bmatrix} \Delta_{1-2} \\ \Delta_{1-3} \\ \vdots \\ \Delta_{1-m} \\ \sum_{i=1}^{m} k_j c_{1,n-1}^{(k)} \end{bmatrix}. \qquad \text{(eq. 1)}$$

Thus, diffusivities, mineral $\delta^{18}O$ zoning profiles, grain-boundary equilibrium fractionations, and flux mass balance are updated with each time step and evolve on the same timescale.

The new FGB code is implemented in a combination of Python and C in order to maintain accessibility and to improve speed. It now also features a GUI to make it more user friendly. Other than the coding language, the major differences between the new and original FGB forward model codes are 1) the ability to implement a multi-segment thermal history with any number of cooling, heating, or isothermal steps, and 2) interactive tables for rapid look-up of experimental fractionation factors and diffusivity parameters, and 3) a fully analytical solution for calculating oxygen isotope flux and grain boundary equilibrium isotopic partitioning at each time step of the simulation. Figure S1 shows a comparison of the output from the original Fortran code and the current Python/C code, demonstrating comparability of results. The user's guide to running the new FGB program is included as part of the supplemental materials and is available on GitHub (see Computer Code Availability) for download along with the new FGB code.

2.2 Inverting the Fast Grain Boundary Model

The inversion of oxygen isotope zoning profiles from one or more minerals grains can be treated as a non-linear optimization problem, solving iteratively with the Levenberg-Marquardt (LM) algorithm (Supplemental Materials). The addition of a regularization (smoothing) term, $\beta \|L\boldsymbol{m}\|_2^2$, to the standard least squares formulation (Aster et al., 2018) prevents overfitting of noisy natural oxygen-isotope zoning datasets:

$$min \sum \left(\frac{G(m_i)-d_i}{\sigma_i}\right)^2 + \beta \|L\boldsymbol{m}\|_2^2 \qquad \text{(eq. 2)}$$

In this equation, $G(m_i)$ are forward modeled mineral $\delta^{18}O$ profiles for a set of model inputs, m; d_i is are actual observed $\delta^{18}O$ profile values; σ_i are the errors on the $\delta^{18}O$ data (see below); β is a smoothing parameter; L is a roughening matrix (see also Supplemental Materials). We use second-order Tikhonov regularization, which penalizes solutions based on the roughness of the second derivative of **m** (Supplemental Materials). A multi-start approach is used to ensure that the solutions are true global minima and not local entrapments. This is determined by rerunning the inverse solver with many different initial solutions, and then comparing all the final solution errors. If there are many equally good solutions (similar errors), then the structure of these solutions is compared to find general trends and make statements about persistent features, such as reheating events.

The FGB program can accept any number of data files corresponding to the diffusive profiles for multiple grains or minerals in a sample. Additionally, if multiple samples are taken from the same region and can be assumed to have experienced the same thermal

history, the program allows these to be combined to more accurately recover the shared thermal history.

Errors (σ_i) or "noise" used in FGB modeling are the total external analytical uncertainties of SIMS $\delta^{18}O$ measurements, as monitored by bracketing measurements of standard materials. For instance, in the real dataset modeled below (section 3.2), the uncertainty assigned to a $\delta^{18}O$ measurement is the standard deviation of measurements of periodically repeated WiscSIMS quartz standard UWQ-1 (Kelly et al., 2007). The reproducibility of a well-known standard value encompasses uncertainties arising from counting statistical errors, random instrumental performance fluctuations, systematic instrumental bias, and random compositional variations in imperfect natural materials. Uncertainties on the equilibrium fractionation factors and diffusivity parameters are not propagated through the FGB modeling, nor are uncertainties resulting from regularization. Users may reduce the effect of uncertainties in equilibrium fractionation factors by using the Vho et al. (2019) internally consistent database of fractionation factors for FGB model construction (Fig. S2).

2.3 Synthetic datasets

Several synthetic datasets are modeled using the LM approach in order to probe the amount of thermal information that can be recorded by and recovered from oxygen isotope zoning (Supplemental Materials). For tests of synthetic datasets, we create a forward model with a known thermal history, select a subset of data points, add noise to the data points, and then run the inverse model to assess thermal history recovery. For each sample scheme, two to four separate noise realizations are generated, and each realization is run 18 times, starting each time from different initial T–t path guess, for a total of 36 to 72 models. The appropriate β smoothing parameter for a given set of tests is determined based on initial L-curve tests (Supplemental Materials; section 4.1) and is fixed. For synthetic data sets, these values are small and range from 0.0056 to 0.02455 (Supplemental Materials). Unless otherwise noted, the synthetic datasets are 'measured' with similar analytical spacing (12 μm) and with similar levels of noise (±0.14‰ 1SD), as the real titanite dataset (Supplemental Materials). The spacing and analytical uncertainties of the real dataset are commonly achievable for in situ oxygen isotope analysis with current SIMS instrumentation and analytical reference materials. These synthetic scenarios provide context for inverse solutions from the real titanite $\delta^{18}O$ data. We explore how the analysis spacing and analytical errors affect the inverse solutions in more detail in the Discussion section.

3. RESULTS

3.1 Summary of inversion results for synthetic data

The synthetic datasets were constructed to test two geologically relevant scenarios – a linear (dT/dt = constant), monotonic cooling history, simulating uninterrupted cooling following orogenic uplift, and a reheating event imposed on a monotonic cooling history, as if orogenic uplift were followed by a magmatic intrusion event.

Inversion of a simple linear cooling T–t path recovers thermal histories that fluctuate about the true history, with alternating cooling and nearly isothermal path segments, but that overall decrease monotonically and at an average rate similar to the true linear cooling rate (Figs. 5A). Decreasing the noise level to 20% of the expected analytical

error produces thermal histories with smaller fluctuations, showing both average and instantaneous cooling rates similar to the true linear cooling rate (Figs. 5B).

Inversion of a thermal spike superimposed on a linear cooling history consistently recovers solutions that show a heating event (Fig. 6). The recovered heating spike is generally broader (1.5-5x longer in duration) and somewhat lower (~25-75°C) than the true heating spike, with these peak distortions showing a correlation such that broader peaks are lower and narrower peaks are higher. The timing and duration of an early heating event (Fig. 6A,B) are recovered more accurately and precisely than the timing and duration of a mid-period or late heating event (Figs. 6C-F). Reducing the analytical uncertainties by half improves recovery of the heating spike timing and the linear cooling segments modestly but does not improve recovery of the heating spike peak (6B,D,F).

In summary, inspection of the synthetic reheating thermal histories (Fig 6) shows that the inversion solver constrains the timing of the heating event somewhat better at lower SIMS analytical uncertainty than is currently available. Nonetheless, comparison of the linear cooling (Fig. 5) and the reheating (Fig. 6) solutions indicates that, at both the current and hypothetical higher levels of analytical precision, the solver can clearly distinguish thermal histories that involve reheating events from those that do not.

3.2 Inversion of real oxygen isotope zoning data from Adirondack titanite

FGB inversion was also tested with real data from Bonamici et al. (2014), who reported intragrain oxygen isotope data from the mineral titanite from the Adirondack Mountains, NY. A subset of the investigated titanite grains were determined to show isotopic zoning formed by diffusion and were forward modeled in an earlier version of the FGB program (Fig. 1). The oxygen isotope zoning profiles were measured in titanite from a metasyenite host rock comprising primarily alkali feldspar, quartz, and augite, with lesser amounts of titanite and iron oxides (Bonamici et al., 2014). Without evidence for a more complex cooling history, Bonamici et al. (2014) fit the oxygen isotope zoning data using simple linear cooling paths, such as those shown in Figure 5. A combination of regional metamorphic constraints and the best model fits suggested cooling from a peak temperature of ~700 °C down to ~500 °C in 2-5 million years (Bonamici et al., 2014). These findings have been used to design both the synthetic and real-data tests for the FGB inversion, providing reasonable starting and ending temperatures, as well as the model durations for the tests.

Oxygen isotope diffusion profiles were measured in several real titanite grains, which are inferred to have shared the same thermal history based on their geologic relations (Bonamici et al., 2014). Combining four diffusion profiles from two different grains results in 102 data points, which are used to reconstruct a discretized, 17-point time-temperature history via inversion. Model results for the real data converge to a nearly linear cooling history for all 18 initial T-t guesses (Fig. 7). Changes in the T–t path slope hint at possible short-lived episodes of more rapid cooling, but there are no indications of reheating events in the samples' history.

4. DISCUSSION

Synthetic and real data presented above establish that the FGB inversion can recover thermal history information from oxygen isotope zoning and, to a first order, distinguish some details within the thermal history. In order to better understand what

information FGB can retrieve and how the resolving power of the models can be improved, we perform additional tests to evaluate the sensitivity of FGB to certain model parameters.

The test procedure follows the approach used for the synthetic thermal histories tests reported in section 3.1 – create a forward model with a known thermal history, select a subset of data points, add noise to the data points, and then run the inverse model to assess thermal history recovery. For each sample scheme, four separate noise realizations are generated, and each realization is run starting from 18 different, random initial-guess T–t paths, for a total of 68 models. The β smoothing parameter is fixed at 0.02455 as described above.

4.1 Effects of regularization on thermal history recovery

To understand the effect of the smoothing parameter, β, on the thermal history recovery, we can compare models run with intentionally low β and "ideal" β values (Fig. 8). Models run with intentionally low β produce an array of T–t paths that have similar shapes (Fig. 8A). These T–t paths correctly reproduce the height and duration of the early heating spike, but they do not agree on its timing. Models run with the optimal β parameter (based on the L-curve topology) (Fig. 8B) show good convergence, with all T–t paths overlapping to place the heating at the correct time; however, the modeled heating spike is both lower and wider than the true spike (Fig. 8C). This result demonstrates the expected trade-offs for regularization: Sensitivity of the model to noisy data is decreased, but some resolution in the recovered T–t paths is lost as the regularization parameter is increased. In as much as natural oxygen isotope data are commonly noisy (see sections 3.1, 4.2) and the timing of a thermal event is often of greater value to geologic interpretation than its absolute magnitude, we conclude that the regularization approach is appropriate.

4.2 Effects of SIMS sampling and analytical uncertainties on thermal history recovery

Two key questions for the FGB inverse modeling revolve around the fundamental ability of secondary ion mass spectrometry oxygen isotope measurements to constrain unique thermal histories. One of these questions is where the most thermal information is preserved in a diffusive oxygen isotope zoning profile. The other is whether the uncertainties on the SIMS measurements are sufficiently small to resolve detailed thermal information in the zoning profile.

Because regularization is built into the inverse model, the question of where thermal information is stored in a profile cannot be addressed directly through minimizing the estimated model covariance matrix. Instead, we test hypothetical analytical schemes with different measurement distances (i.e., spacing between SIMS analysis pits), different measurement locations (i.e., near grain margins versus grain centers), and measurement precisions (i.e., isotope analysis uncertainties) to track the behavior of the inverse model as a function of these analytical parameters (Fig. 9). The first four analysis schemes utilize the current state-of-the-art for analytical spacing and uncertainty for a 10-μm SIMS analysis of $\delta^{18}O$ (Kita et al., 2009). The subsequent four analytical schemes explore the potential improvements to inverse thermal history recovery that might be achieved through closer analytical spacing, different analysis locations, and/or higher precision oxygen isotope measurements.

The first analytical scheme tests measurements on a single side of the oxygen isotope diffusion profile near the grain margin (Figs. 9A, S5). The inversion generally retrieves a heating event early in the T–t history and an approximately linear cooling trend

later in the *T*–*t* history but does not strongly constrain the height of the heating event or its duration. Only one acceptable model solution shows no reheating event at all.

The second analytical scheme tests a smaller set of measurements spanning only part of the isotope gradient but on both sides of the diffusion profile (Figs. 9B, S6). Because the isotope profile is symmetric, this effectively cuts the number of measurements in half and reduces their uncertainty by a factor of $\sqrt{2}$. Again, while most solutions recover an early heating event, the height and duration of the heating event are not well constrained, and the model produces more variable results for the second half of the *T*–*t* history. Two acceptable model solutions show no reheating event at all.

For analytical scheme 3, measurements are taken near the center of the isotope profile (Figs. 9C, S7). This scheme nicely recovers the height and duration of the heating event in almost all acceptable model solutions; however, the timing of the reheating event is very poorly constrained, and no portion of the linear cooling trend is correctly recovered.

Analytical scheme 4 combines measurements taken near the grain margin with measurements near the grain center (Figs. 9D, S8). The resulting *T*–*t* histories show some improvement over the solutions for scheme 1 in their ability to more consistently recover the peak reheating temperature and the reheating duration. This suggests that Scheme 1 stopped just short of measuring $\delta^{18}O$ values most representative of the grain core. Thus, SIMS analyses that sample $\delta^{18}O$ representative of the grain center ensures the best recovery of peak thermal conditions. However, several of the acceptable solutions – especially those for noise realization 1 – show a combination of somewhat low peak reheating temperatures and secondary reheating events, rather than the correct linear cooling.

Analytical schemes 5 through 8 test scenarios mirror the placement of SIMS measurements in schemes 1 through 4 but with closer analytical spacing or improved analytical precision, or both. Broadly, comparing the first four sampling schemes to the second four sampling schemes, more of the acceptable *T*–*t* paths converge and overlap for a given noise realization in schemes 5-8 (with the exception of scheme 6, discussed below). This improved convergence indicates that higher sampling density and better analytical precision decrease the sensitivity of the inversion results to the initial-guess *T*–*t* path.

Inspection of the individual schemes provides additional insights into the model performance. The closer analysis spacing in scheme 5 yields consistent solutions that tend to place the reheating event early and recover the correct reheating duration but still sometimes underestimates the peak reheating temperature (Figs. 9E, S9). The more closely spaced, high-precision measurements at the grain center in scheme 6 (Figs. 9F, S10) do not improve on the solutions recovered with more widely spaced and less precise grain-center analyses in scheme 3 (Figs. 9C). This is consistent with the previous conclusion that grain centers primarily preserve information about the earlier, higher-temperature parts of thermal histories and little information about the later, lower-temperature parts of thermal histories. Thus, improved SIMS analytical precision and sampling density are of little use if the portion of the diffusion profile with the most thermal information near the grain margin is not sampled. The high-precision sampling scheme 7 consistently recovers the early timing of the reheating event and constrains reheating duration but commonly underestimates the peak reheating temperature (Figs. 9G, S11). Thus, scheme 7 is a modest improvement on scheme 1 (Fig. 9A). Similarly, scheme 8 (Fig. 9H) offers a modest

improvement on scheme 4 (Fig. 9D), showing more consistent recovery of the early timing of the reheating event, as well as fewer and smaller spurious secondary reheating events.

The natural titanite data modeled in section 3.2 were collected using analytical parameters closely resembling those of the scheme 1 and scheme 4 synthetic tests (Figs. 9A, 9D). Considered in light of the synthetic test results, we have a high confidence that the nearly monotonic cooling history recovered for these samples is accurate and that there were no significant thermal fluctuations during the temperature-time interval preserved in the natural titanite $\delta^{18}O$ data.

4.3 Non-uniqueness in the in the inverse problem for *T*–*t* histories

Total diffusive mass flux for a given mineral depends primarily on the amount of time the mineral spends in its partial retention zone (PRZ) – the range of temperatures where diffusion is an efficient mechanism of mass transport at the scale of the mineral grain. Diffusion is very efficient at temperatures on the high end of the PRZ and becomes exponentially less efficient with decreasing temperature. As such, similar diffusive fluxes, and thus similar diffusion profiles, can be achieved by a little time spent at higher temperature or a longer time spent at lower temperature. Consequently, inversions of diffusion data can fall into global, but flat-bottomed minima, where model solutions are insensitive to several model parameters that one might hope to constrain.

In the synthetic tests presented here (Figs. 6, 9), this non-uniqueness in the inverse problem is likely the reason that the best model results can only constrain the timing of the reheating events to within ~2-3 million years of its true position. Spurious fluctuations in the modeled T-t histories may reflect the combination of non-uniqueness in the diffusion problem and noise in the $\delta^{18}O$ data used for inversion. Nonetheless, it should be noted that resolution of thermal events on the scale of 2 million years can be useful and, in many cases, represents a large improvement over existing constraints on thermal histories for many geologic terranes.

4.4 Fluid, microstructure, and applicability of the FGB diffusion model

The FGB model assumes that the rock microstructure is fixed and that all oxygen isotope exchange within a rock system occurs via diffusion over the modeled time period. This is unrealistic for rocks experiencing reactions and/or fluid-assisted, deformation-assisted, or static recrystallization, during which the breaking and reforming of bonds facilitates oxygen isotope exchange (e.g., Cole and Chakraborty, 2001). Reaction- and recrystallization-induced changes to the topology of the grain-boundary network should have little or no effect on fast oxygen isotope transport and rapid $\delta^{18}O$ equilibration along grain boundaries (e.g., Farver and Yund 1991), provided that the grain boundaries maintain interconnectivity. Eiler et al. (1995) demonstrated that even in coarse-grained, water-poor rocks, rapid (effectively instantaneous) grain-boundary $\delta^{18}O$ equilibration was achieved at the scale of a hand sample. Recrystallization that reduces grain size and increases grain boundary area will only increase the rate of grain boundary equilibration. More importantly for applying the FGB model, changes in grain size and shape during reactions and recrystallization can alter the diffusion domain size and shape, affecting the rate of isotope exchange between grain interiors and grain boundaries, as well as the diffusion profiles that develop. Thus, careful characterization of the rock microstructure and analysis of overall mineral zoning patterns is required to determine whether intragrain oxygen isotope zoning can be credibly modeled with FGB.

5. CONCLUSIONS

1) The Fast Grain Boundary model can be inverted to recover time-temperature paths from oxygen isotope zoning in minerals. The temporal and thermal resolution of the inverted *T*–*t* histories will be fundamentally limited by non-uniqueness in the diffusion equations; however, tests of the FGB inversion suggest that details in the *T*–*t* histories of geological samples can be recovered at a resolution of 2-3 million years and within 25-50 °C.

2) For the purposes of inverse thermal history modeling, the greatest amount of thermal history information is preserved in the oxygen-isotope gradients toward grain margins, but sampling of grain interiors is necessary to locate thermal maxima (if any) experienced by samples.

3) Inversion of $\delta^{18}O$ zoning profiles from real Adirondack titanite grains show a monotonic cooling history with no significant thermal perturbations.

4) Inverse modelling tests suggest that thermal history recovery will be most improved by careful placement of SIMS $\delta^{18}O$ measurements and slightly improved by better SIMS analytical precision. Ideally, SIMS $\delta^{18}O$ measurements should extend from grain rim to grain center with the closest possible spacing for the best-constrained inversion results. When combined with a careful sampling strategy, a 2x reduction of the SIMS analytical uncertainty will reduce spurious modeled *T*–*t* path fluctuations. A reduction in SIMS analytical uncertainties will be most accessible through development of high-precision microanalytical standards for $\delta^{18}O$, as standard reproducibility is currently the major contributor to SIMS $\delta^{18}O$ analytical uncertainty (Valley and Kita, 2009).

ACKNOWLEDGEMENTS

The authors thank John Eiler and John Valley for permission to re-work the FGB program. We thank Andrew Smye, Pierre Lanari, and an anonymous reviewer for helpful critiques. This material is based upon work supported by the National Science Foundation Grant No. EAR 1650355.

COMPUTER CODE AVAILABILITY

The Fast Grain Boundary Diffusion Solver was developed by Gabriel Kropf and was first made available on GitHub in 2018. It can be directly downloaded (4 MB) from https://github.com/gkropf/FastGrainBoundary-DiffusionSolver. The FGB code is written in Python and C; it can be run on any personal computer with Python 3 and the tkinter, numpy, scipy, matplotlib, pandas, glob, and os packages. We recommend the Anaconda distribution of Python 3.7, which includes all of these packages. Questions about the code and availability can be directed to Gabriel Kropf via Github or to corresponding author Chloë Bonamici at the Department of Geoscience, University of Wisconsin-Madison, Madison, WI 53706; telephone +1 (608) 263-7754; email: bonamici@wisc.edu.

FIGURES

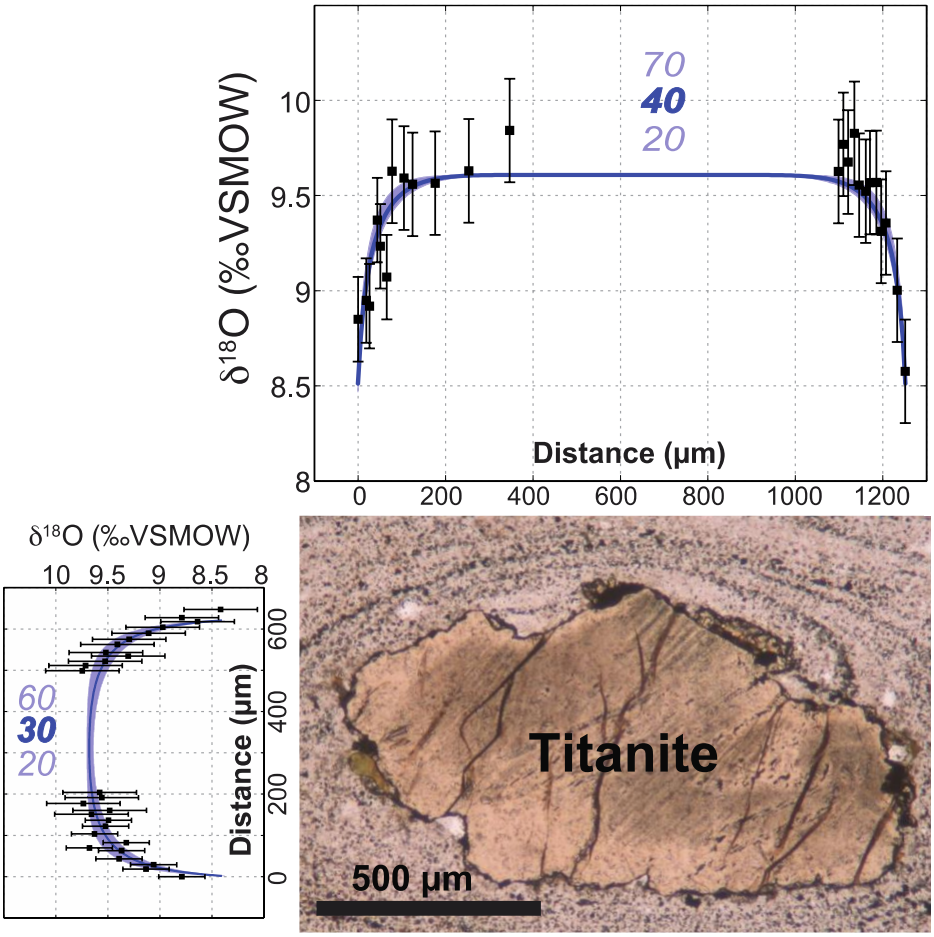

Figure 1. Oxygen isotope variations (zoning) in titanite revealed by secondary ion mass spectrometry measurements collected along traverses across a titanite grain (black squares and error bars). Blue bands show Fast Grain Boundary forward model fits to the oxygen isotope data, assuming strictly monotonic linear cooling (dT/dt = constant). Acceptable cooling rates (in °C/m.y.) based on the linear cooling models are given in blue numbers, with the best-fit linear cooling rate in bold.

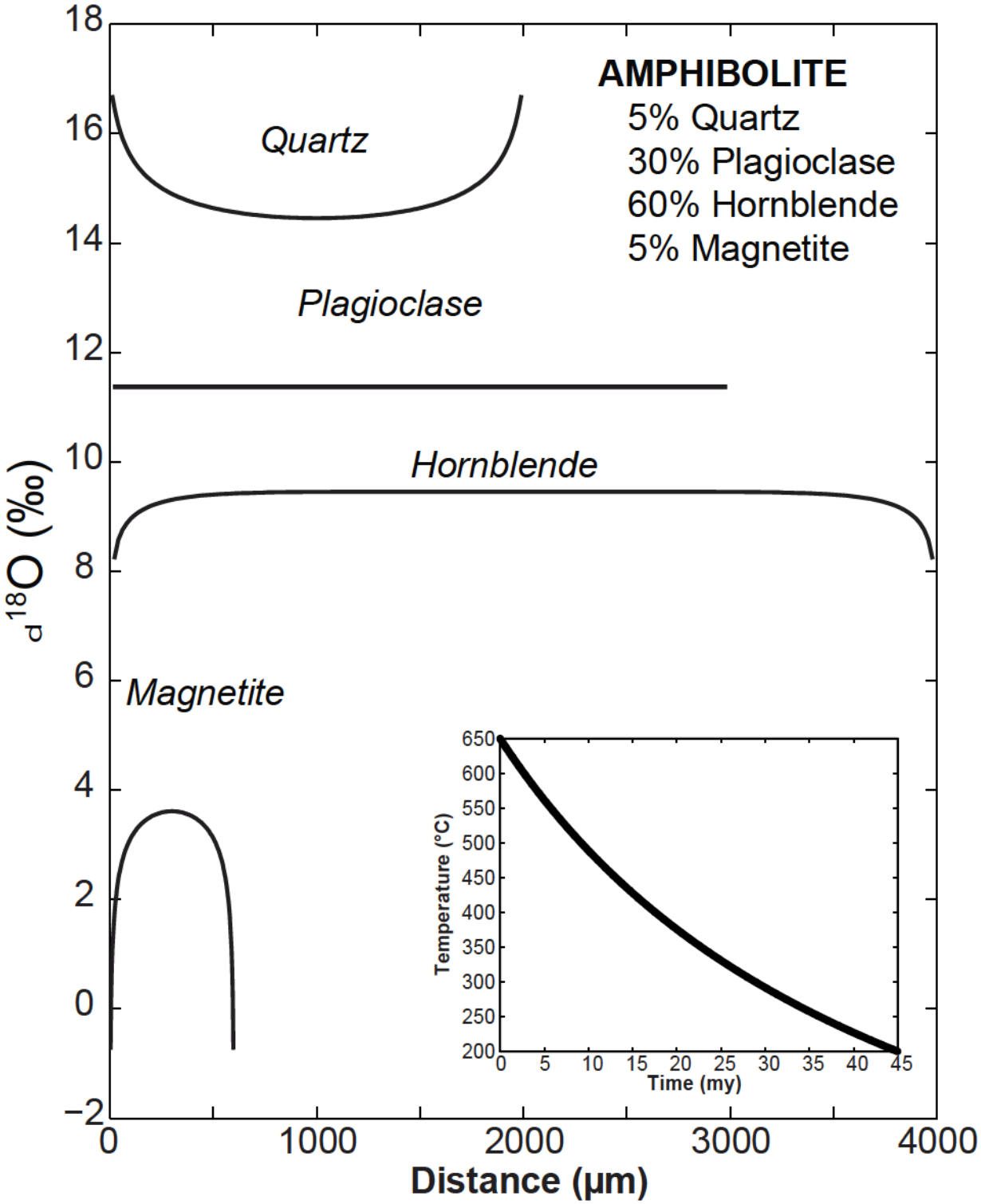

Figure 2. FGB forward model of oxygen isotope zoning that will result from diffusive oxygen isotope exchange in a hypothetical amphibolite. Minerals and modes are shown in the upper righthand corner. Mineral sizes are indicated by distances along the x axis. Modeled temperature-time history is shown in the lower right inset.

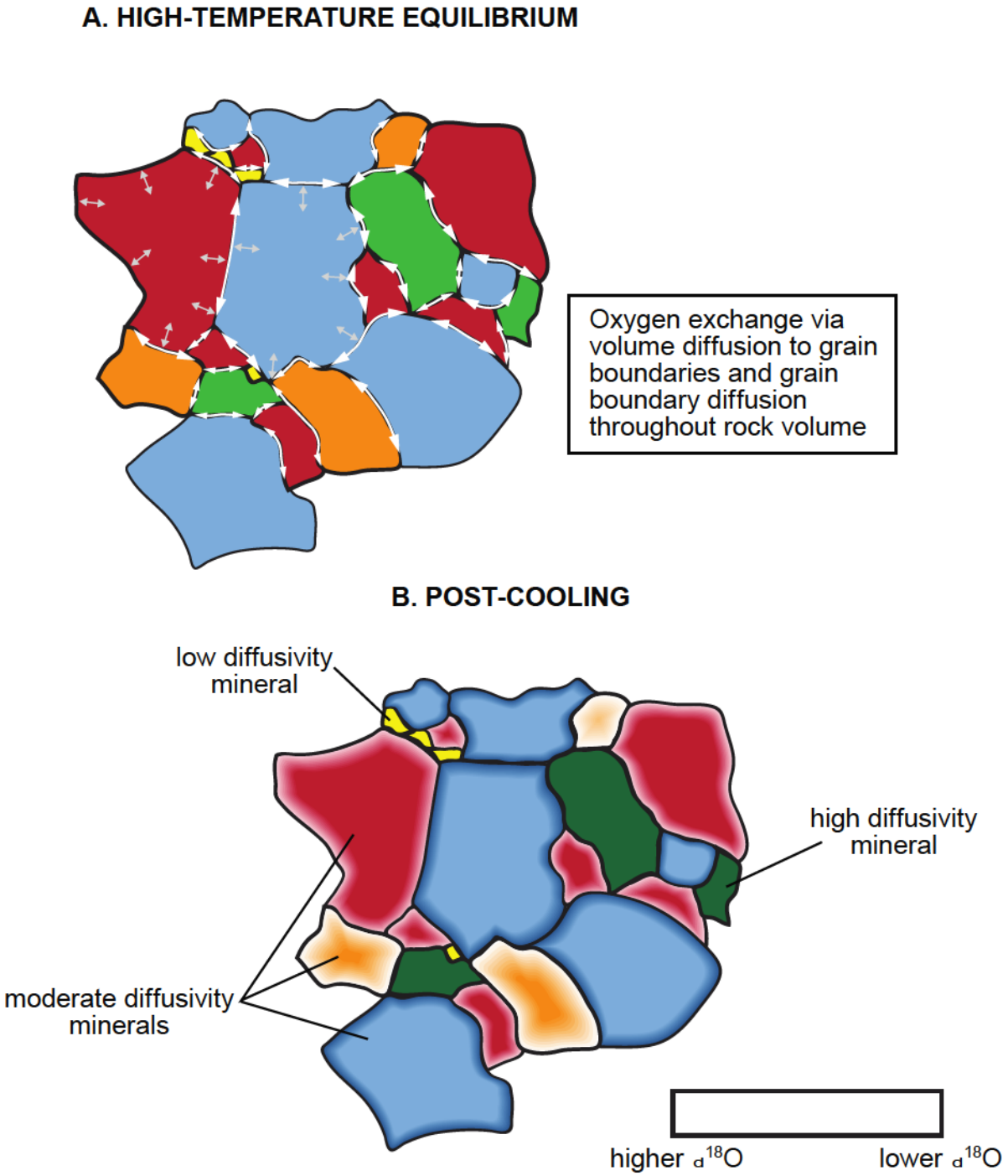

Figure 3. Cartoon illustrating the oxygen isotope zoning that develops in mineral grains as a result of diffusive oxygen flux in response to changing temperature in the Fast Grain Boundary model. Arrows in top diagram show that diffusion is fast along grain boundaries and much slower within grain interiors.

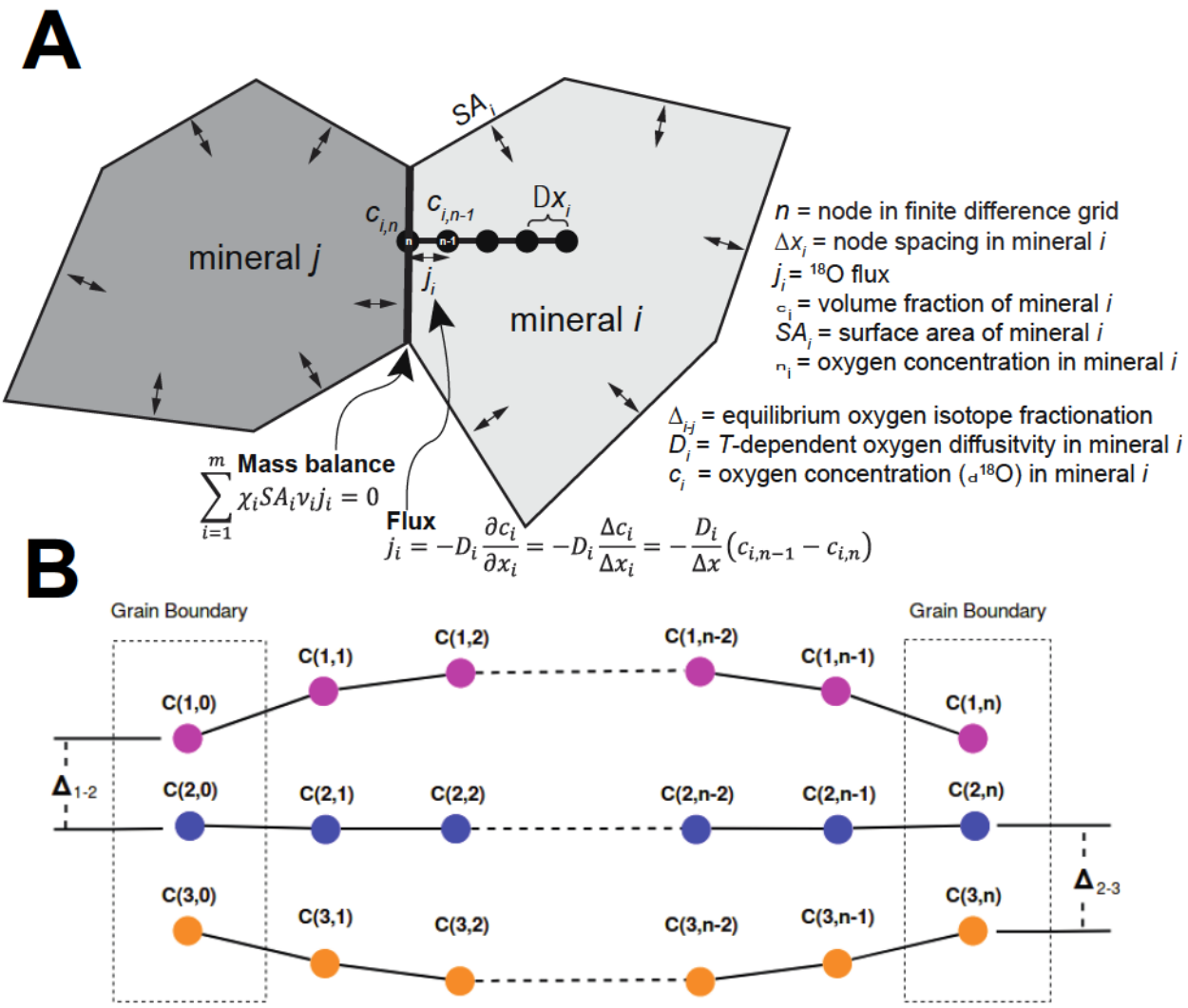

Figure 4. Schematic diagrams showing how oxygen isotope flux and oxygen isotope equilibrium fractionation are coupled in the Fast Grain Boundary model. (A) Diagram demonstrating the flux balance calculation at the grain boundary. (B) Schematic diagram of distance versus concentration showing the spatially discretized representation of an oxygen isotope zoning profile with the grain boundary node concentrations determined by equilibrium oxygen isotope fractionations. Upper concentration profile shows a mineral that loses 18O with decreasing temperature. The lower concentration profile shows a mineral that gains 18O with decreasing temperature.

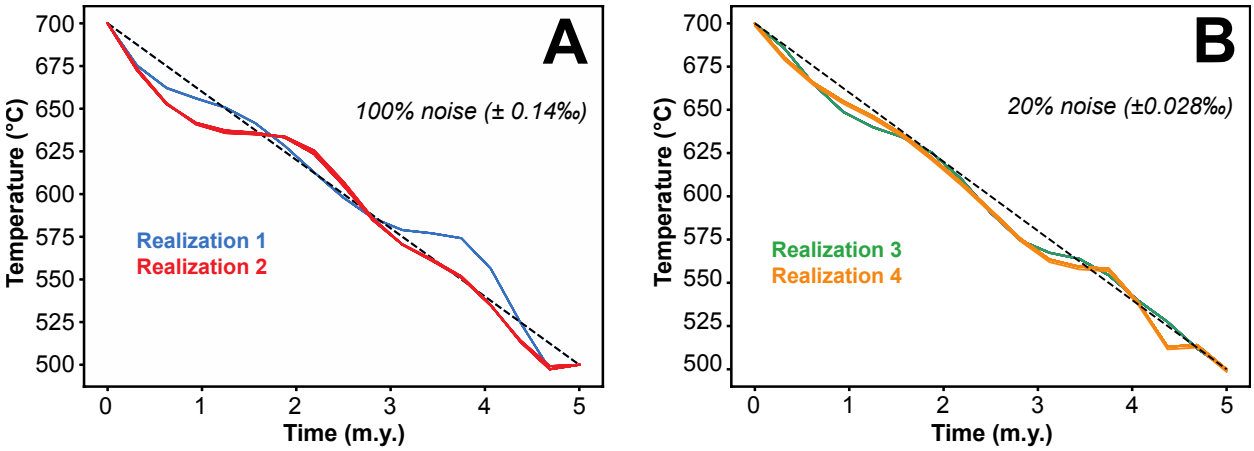

Figure 5. Inverse model solutions for a simple synthetic linear cooling history with (A) full noise (typical 1s analytical errors for SIMS oxygen isotope analysis) and (B) 20% of full noise. Black dashed line is the true cooling history. Color curves are the model-recovered T–t paths. Regularization collapses similar solutions so that the 36 acceptable solutions (18 per noise realization) in each panel overlap and appear as only two T–t paths.

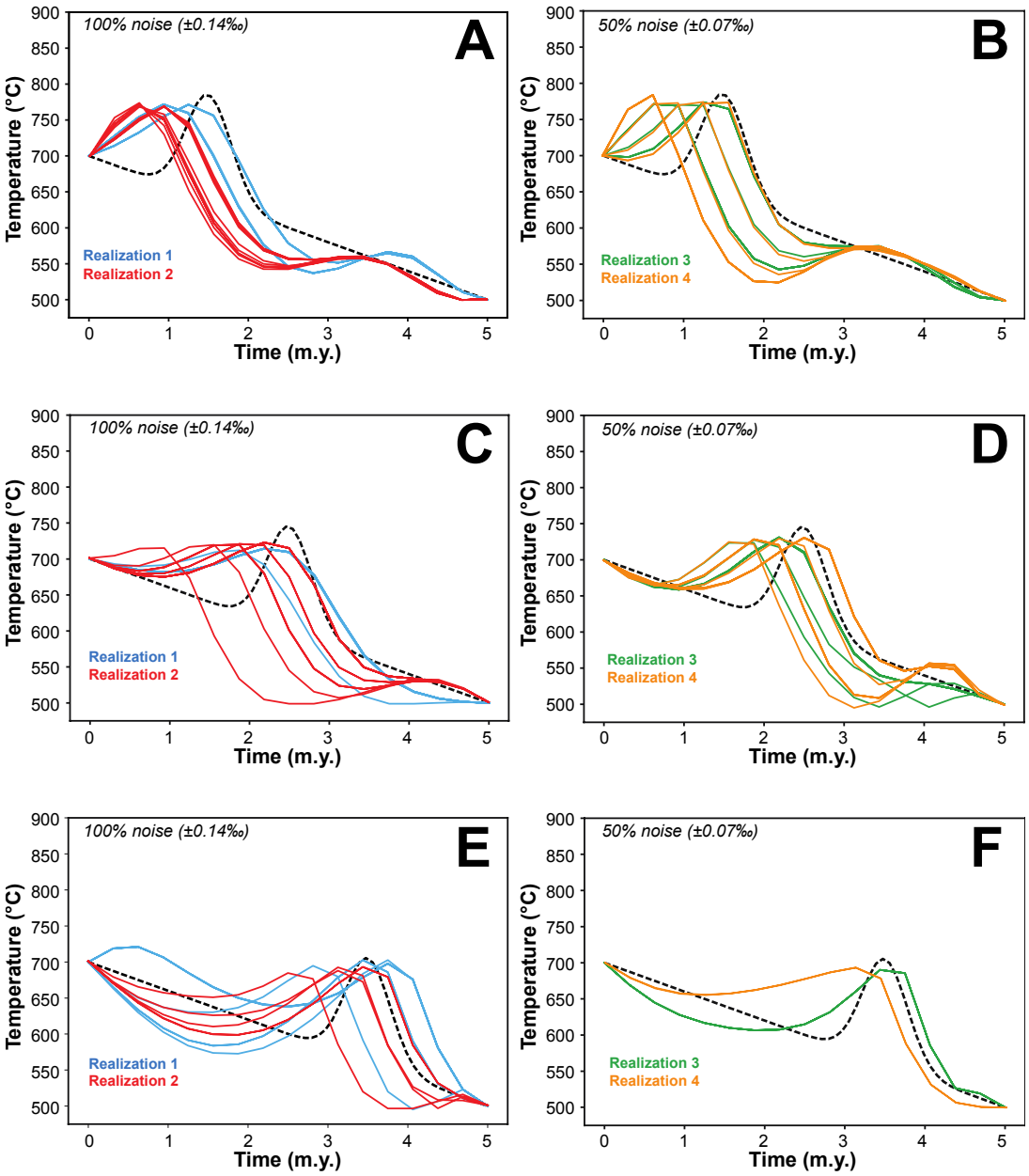

Figure 6. Inverse model solutions for a synthetic data sets that include a heating spike during cooling. (A,B) Early heating spike with 100% and 50% of current SIMS analytical uncertainty, respectively. (C,D) Middle-period heating spike with 100% and 50% of current SIMS analytical uncertainty, respectively. (E,F) Late heating spike with 100% and 50% of current SIMS analytical uncertainty, respectively. Black dashed lines are the true cooling histories. Color curves are acceptable model-recovered T–t paths. Each set of models includes four noise realizations and 18 random starts for each realization. Only accepted solutions (those with total misfit <1% above the minimum misfit for all model solutions) are shown. Regularization collapses similar solutions so that the 36 acceptable solutions (18 per noise realization) in each panel overlap and appear as fewer T–t paths. See Supplemental Material for details of accepted solutions.

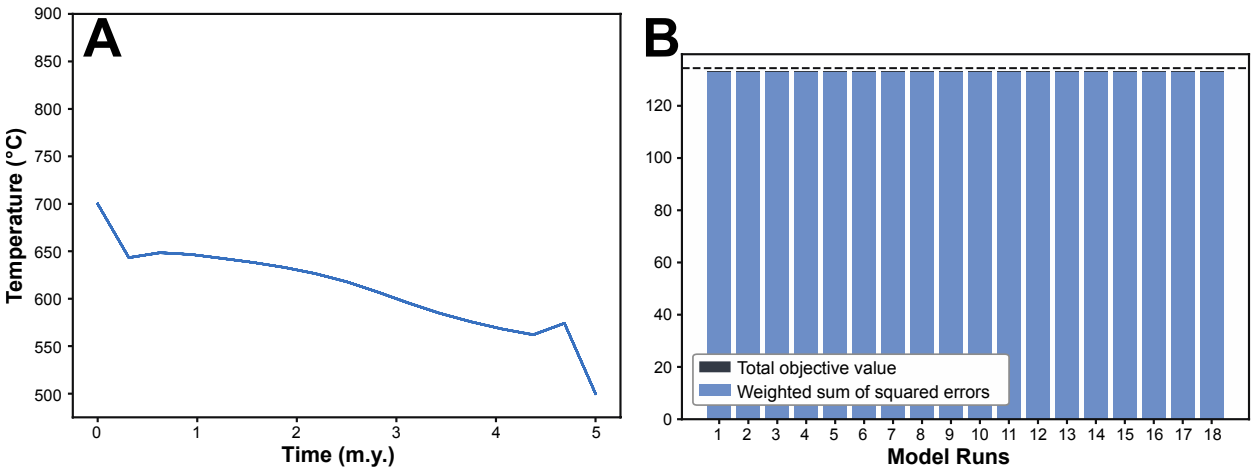

Figure 7. Inversion results from for real titanite oxygen isotope zoning data from the Adirondack Mountains. Four $\delta^{18}O$ zoning profiles from two different grains were inverted jointly. (A) Model-recovered *T*–*t* paths from all 18 model runs with different random starts. Regularization collapses similar solutions so that the 18 acceptable solutions overlap and appear as only one T-t path. (B) Model misfits for each run. Dashed line shows the cut-off for an acceptable solution at 1% above the minimum misfit of all models. Errors in the models are essentially identical because of non-uniqueness of the error of the solution.

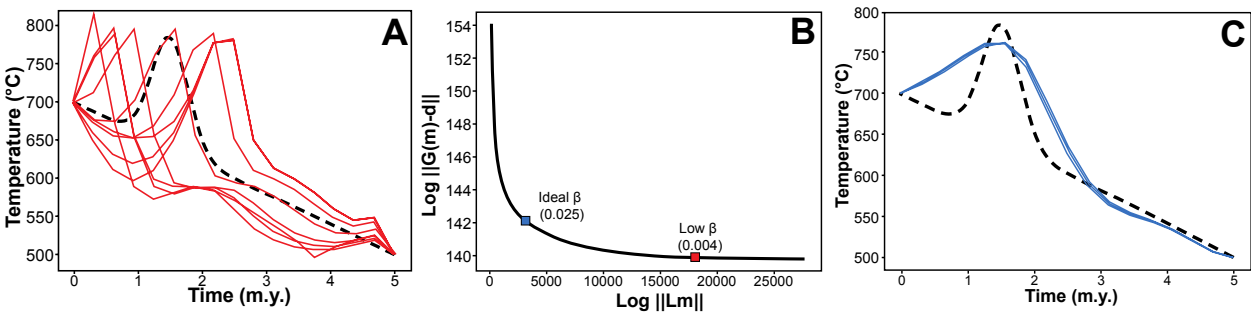

Figure 8. Comparison of model results for an early heating spike T–t history using low and ideal regularization (smoothing) parameters. (A) Model solutions for under-regularized problem with β = 0.004. (B) L-curve showing the relative positions of the β parameters used in regularization tests. (C) Model solutions for well-regularized problem with β = 0.025. Black dashed line is the true cooling history. Color curves are model-recovered T–t paths.

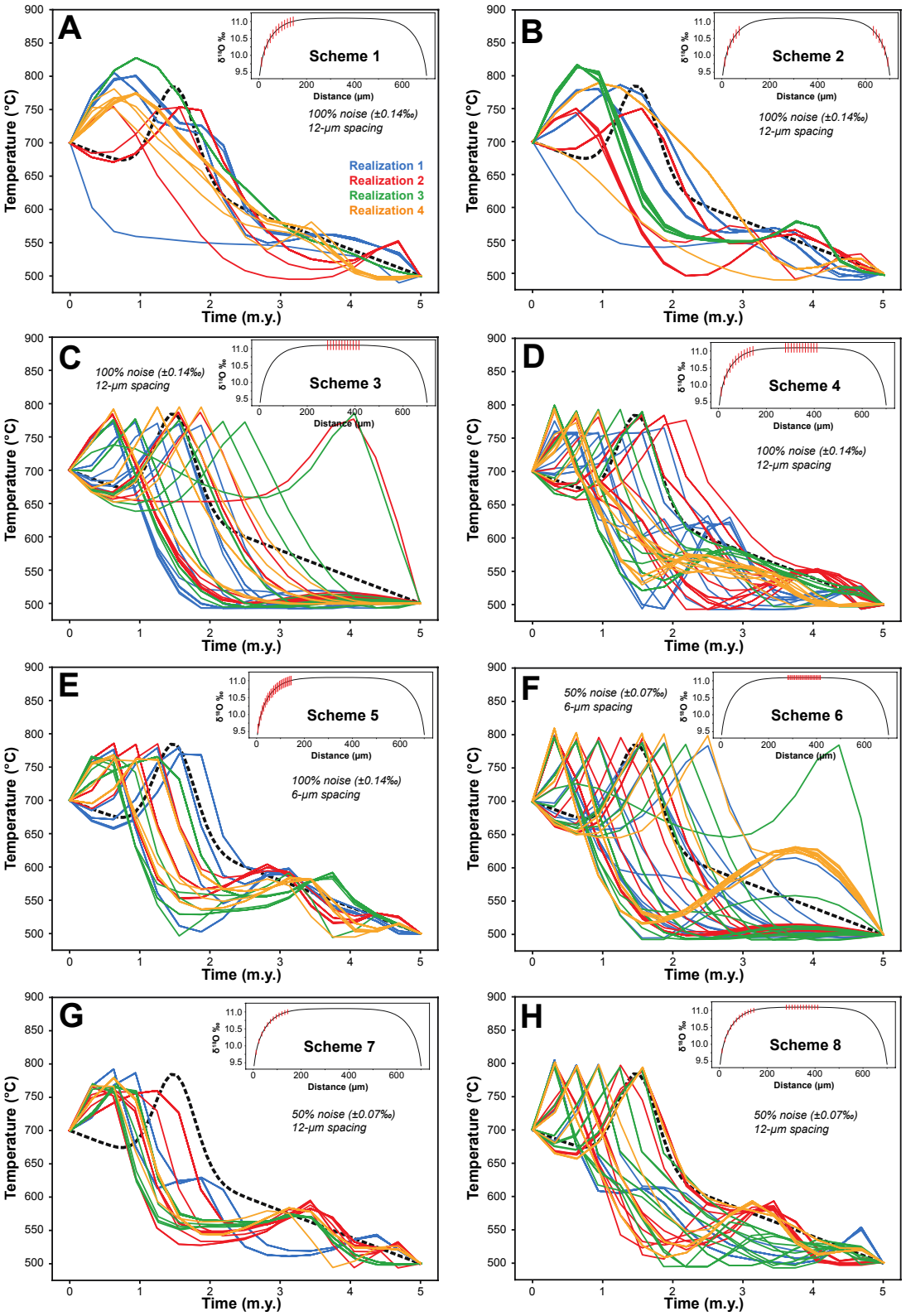

Figure 9. Models of synthetic datasets testing the effects of SIMS analysis spacing and analytical uncertainty on thermal history recovery. For each test, inset schematically shows the SIMS analysis locations and uncertainty with the spacing and length of red bars,

respectively. (A) Scheme 1: sampling one side of profile with 12-μm spacing and current analytical precision (±0.14‰ 1SD). (B) Scheme 2: partially sampling both sides of profile with 12-μm spacing and current analytical precision (±0.14‰). (C) Scheme 3: sampling center of profile with 12-μm spacing and current analytical precision (±0.14‰). (D) Scheme 4: sampling one side and center of profile with 12-μm spacing and current analytical precision (±0.14‰). (E) Scheme 5: sampling one side of profile with 6-μm spacing and current analytical precision (±0.14‰). (F) Scheme 6: sampling center of profile with 6-μm spacing and 50% of current analytical precision (±0.07‰). (G) Scheme 7: sampling one side of profile with 12-μm spacing and 50% of current analytical precision (±0.07‰). (H) Scheme 8: sampling one side and center of profile with 12-μm spacing and 50% of current analytical precision (±0.07‰). Black dashed line is the true cooling history. Colored lines are acceptable model-recovered T–t paths. Each set of models includes four noise realizations and 18 random starts for each realization. Only accepted solutions (those with total misfit <1% above the minimum misfit for all model solutions) are shown. Regularization collapses similar solutions so that the 72 acceptable solutions (18 per noise realization) in each panel overlap and appear as fewer T–t paths. See Supplemental Material for details of accepted solutions.

REFERENCES CITED

Aster, R.C., Borchers, B., Thurber, C.H., 2018. Parameter Estimation and Inverse Problems. Elsevier.

Bindeman, I.N., Fu, B., Kita, N.T., Valley, J.W., 2008. Origin and Evolution of Silicic Magmatism at Yellowstone Based on Ion Microprobe Analysis of Isotopically Zoned Zircons. J Petrology 49, 163–193. https://doi.org/10.1093/petrology/egm075

Bonamici, C.E., 2013. From grain to terrane: Integrated geochemical and structural studies in granulites (Ph.D.). The University of Wisconsin - Madison, United States -- Wisconsin.

Bonamici, C.E., Kozdon, R., Ushikubo, T., Valley, J.W., 2014. Intragrain oxygen isotope zoning in titanite by SIMS: Cooling rates and fluid infiltration along the Carthage-Colton Mylonite Zone, Adirondack Mountains, NY, USA. J. Meta. Geol. 32, 71–92. https://doi.org/10.1111/jmg.12059

Britz, D., Østerby, O., Strutwolf, J., 2003. Damping of Crank–Nicolson error oscillations. Computational Biology and Chemistry 27, 253–263. https://doi.org/10.1016/S0097-8485(02)00075-X

Chacko, T., Cole, D.R., Horita, J., 2001. Equilibrium Oxygen, Hydrogen and Carbon Isotope Fractionation Factors Applicable to Geologic Systems. Reviews in Mineralogy and Geochemistry 43, 1–81. https://doi.org/10.2138/gsrmg.43.1.1

Cherniak, D.J., 1993. Lead diffusion in titanite and preliminary results on the effects of radiation damage on Pb transport. Chemical Geology, Geochemistry of Accessory Minerals 110, 177–194. https://doi.org/10.1016/0009-2541(93)90253-F

Cole, D.R., Chakraborty, S., 2001. Rates and Mechanisms of Isotopic Exchange. Reviews in Mineralogy and Geochemistry 43, 83–223. https://doi.org/10.2138/gsrmg.43.1.83

Crank, J., 1975. The Mathematics of Diffusion. Clarendon Press.

Dodson, M.H., 1986. Closure Profiles in Cooling Systems [WWW Document]. Materials Science Forum. https://doi.org/10.4028/www.scientific.net/MSF.7.145

Dodson, M.H., 1973. Closure temperature in cooling geochronological and petrological systems. Contr. Mineral. and Petrol. 40, 259–274. https://doi.org/10.1007/BF00373790

Eiler, J.M., Baumgartner, L.P., Valley, J.W., 1994. Fast grain boundary: A FORTRAN-77 program for calculating the effects of retrograde interdiffusion of stable isotopes. Computers & Geosciences 20, 1415–1434. https://doi.org/10.1016/0098-3004(94)90102-3

Eiler, J.M., Baumgartner, L.P., Valley, J.W., 1992. Intercrystalline stable isotope diffusion: a fast grain boundary model. Contributions to Mineralogy and Petrology 112, 543–557. https://doi.org/10.1007/bf00310783

Eiler, J.M., Valley, J.W., Baumgartner, L.P., 1993. A new look at stable isotope thermometry. Geochimica et Cosmochimica Acta 57, 2571–2583. https://doi.org/10.1016/0016-7037(93)90418-V

Eiler, J.M., Valley, J.W., Graham, C.M., Baumgartner, L.P., 1995. The oxygen isotope anatomy of a slowly cooled metamorphic rock. American Mineralogist 80, 757–764. https://doi.org/10.2138/am-1995-7-813

England, P.C., Thompson, A.B., 1984. Pressure—Temperature—Time Paths of Regional Metamorphism I. Heat Transfer during the Evolution of Regions of Thickened Continental Crust. J Petrology 25, 894–928. https://doi.org/10.1093/petrology/25.4.894

Farver, J.R., 2010. Oxygen and Hydrogen Diffusion in Minerals. Reviews in Mineralogy and Geochemistry 72, 447–507. https://doi.org/10.2138/rmg.2010.72.10

Farver, J.R., 1989. Oxygen self-diffusion in diopside with application to cooling rate determinations. Earth and Planetary Science Letters 92, 386–396. https://doi.org/10.1016/0012-821X(89)90062-9

Farver, J.R., Yund, R.A., 1991. Measurement of oxygen grain boundary diffusion in natural, fine-grained, quartz aggregates. Geochimica et Cosmochimica Acta 55, 1597–1607. https://doi.org/10.1016/0016-7037(91)90131-N

Gallagher, K., 2012. Transdimensional inverse thermal history modeling for quantitative thermochronology. Journal of Geophysical Research: Solid Earth 117. https://doi.org/10.1029/2011jb008825

Harrison, T.M., Grove, M., Lovera, O.M., Zeitler, P.K., 2005. Continuous Thermal Histories from Inversion of Closure Profiles. Reviews in Mineralogy and Geochemistry 58, 389–409. https://doi.org/10.2138/rmg.2005.58.15

Holder, R.M., Sharp, Z.D., Hacker, B.R., 2018. LinT, a simplified approach to oxygen-isotope thermometry and speedometry of high-grade rocks: An example from ultrahigh-temperature gneisses of southern Madagascar. Geology 46, 931–934. https://doi.org/10.1130/G40207.1

Jenkin, G.R.T., Fallick, A.E., Farrow, C.M., Bowes, G.E., 1991. COOL: A FORTRAN-77 computer program for modeling stable isotopes in cooling closed systems. Computers & Geosciences 17, 391–412. https://doi.org/10.1016/0098-3004(91)90047-H

Jenkin, G.R.T., Farrow, C.M., Fallick, A.E., Higgins, D., 1994. Oxygen isotope exchange and closure temperatures in cooling rocks. Journal of Metamorphic Geology 12, 221–235. https://doi.org/10.1111/j.1525-1314.1994.tb00018.x

Kelly, J.L., Fu, B., Kita, N.T., Valley, J.W., 2007. Optically continuous silcrete quartz cements of the St. Peter Sandstone: High precision oxygen isotope analysis by ion microprobe. Geochimica et Cosmochimica Acta 71, 3812–3832. https://doi.org/10.1016/j.gca.2007.05.014

Ketcham, R.A., 2005. Forward and Inverse Modeling of Low-Temperature Thermochronometry Data. Reviews in Mineralogy and Geochemistry 58, 275–314. https://doi.org/10.2138/rmg.2005.58.11

Kirkland, C.L., Hollis, J., Danišík, M., Petersen, J., Evans, N.J., McDonald, B.J., 2017. Apatite and titanite from the Karrat Group, Greenland; implications for charting the thermal evolution of crust from the U-Pb geochronology of common Pb bearing phases. Precambrian Research 300, 107–120. https://doi.org/10.1016/j.precamres.2017.07.033

Kita, N.T., Ushikubo, T., Fu, B., Valley, J.W., 2009. High precision SIMS oxygen isotope analysis and the effect of sample topography. Chemical Geology 264, 43–57. https://doi.org/10.1016/j.chemgeo.2009.02.012

Lovera, O.M., Grove, M., Harrison, T.M., 2002. Systematic analysis of K-feldspar 40Ar/39Ar step heating results II: relevance of laboratory argon diffusion properties to nature. Geochimica et Cosmochimica Acta 66, 1237–1255. https://doi.org/10.1016/S0016-7037(01)00846-8

Lovera, O.M., Grove, M., Mark Harrison, T., Mahon, K.I., 1997. Systematic analysis of K-feldspar 40Ar/39Ar step heating results: I. Significance of activation energy determinations. Geochimica et Cosmochimica Acta 61, 3171–3192. https://doi.org/10.1016/S0016-7037(97)00147-6

Rubin, A.E., Cooper, K.M., Till, C.B., Kent, A.J.R., Costa, F., Bose, M., Gravley, D., Deering, C., Cole, J., 2017. Rapid cooling and cold storage in a silicic magma reservoir recorded in individual crystals. Science 356, 1154–1156. https://doi.org/10.1126/science.aam8720

Smye, A.J., Marsh, J.H., Vermeesch, P., Garber, J.M., Stockli, D.F., 2018. Applications and limitations of U-Pb thermochronology to middle and lower crustal thermal histories. Chemical Geology 494, 1–18. https://doi.org/10.1016/j.chemgeo.2018.07.003

Smye, A.J., Stockli, D.F., 2014. Rutile U–Pb age depth profiling: A continuous record of lithospheric thermal evolution. Earth and Planetary Science Letters 408, 171–182. https://doi.org/10.1016/j.epsl.2014.10.013

Stearns, M.A., Hacker, B.R., Ratschbacher, L., Rutte, D., Kylander-Clark, A.R.C., 2015. Titanite petrochronology of the Pamir gneiss domes: Implications for middle to deep crust exhumation and titanite closure to Pb and Zr diffusion. Tectonics 34, 784–802. https://doi.org/10.1002/2014TC003774

Storm, L.C., Spear, F.S., 2005. Pressure, temperature and cooling rates of granulite facies migmatitic pelites from the southern Adirondack Highlands, New York. Journal of Metamorphic Geology 23, 107–130. https://doi.org/10.1111/j.1525-1314.2005.00565.x

Urey, H.C., 1948. Oxygen Isotopes in Nature and in the Laboratory. Science 108, 489–496.

Urey, H.C., 1947. The thermodynamic properties of isotopic substances. J Chem Soc 562–581. https://doi.org/10.1039/jr9470000562

Valley, J.W., 2001. Stable Isotope Thermometry at High Temperatures. Reviews in Mineralogy and Geochemistry 43, 365–413. https://doi.org/10.2138/gsrmg.43.1.365

Valley, J.W., Kita, N.T., 2009. In situ oxygen isotope geochemistry by ion microprobe. Mineralogical Society of Canada Short Course Series 41, 19–63.

Vho, A., Lanari, P., Rubatto, D., 2019. An Internally-Consistent Database for Oxygen Isotope Fractionation Between Minerals. J Petrology 60, 2101–2129. https://doi.org/10.1093/petrology/egaa001

Warren, C.J., Grujic, D., Cottle, J.M., Rogers, N.W., 2012. Constraining cooling histories: rutile and titanite chronology and diffusion modelling in NW Bhutan. Journal of Metamorphic Geology 30, 113–130. https://doi.org/10.1111/j.1525-1314.2011.00958.x

Watson, E.B., Cherniak, D.J., 2015. Quantitative cooling histories from stranded diffusion profiles. Contrib Mineral Petrol 169, 1–14. https://doi.org/10.1007/s00410-015-1153-4

Watts, K.E., Bindeman, I.N., Schmitt, A.K., 2012. Crystal scale anatomy of a dying supervolcano: an isotope and geochronology study of individual phenocrysts from voluminous rhyolites of the Yellowstone caldera. Contrib Mineral Petrol 164, 45–67. https://doi.org/10.1007/s00410-012-0724-x

Wolf, R.A., Farley, K.A., Kass, D.M., 1998. Modeling of the temperature sensitivity of the apatite (U–Th)/He thermochronometer. Chemical Geology 148, 105–114. https://doi.org/10.1016/S0009-2541(98)00024-2

SUPPLEMENTAL MATERIALS

A. Details of the updated Fast Grain Boundary numerical model

Diffusive exchange of oxygen between mineral phases in the model rock is driven by temperature variations, which are imposed through finite time steps and the time-temperature relationship, *T(t),* set by the user. At each time step, the temperature is updated through the T(t) function, as are the temperature-dependent equilibrium fractionations, $\Delta_{i\text{-}j}(T)$, and diffusivity, $D(T)$, for each mineral (Fig. 4). The equilibrium oxygen isotope fractionation between two minerals (generically designated *i* and *h*) is calculated as

$$\Delta_{i-h} = \delta^{18}O_i - \delta^{18}O_h \approx A_{i-h} + B_{i-h}\frac{10^3}{T} + C_{i-h}\frac{10^6}{T^2} \qquad \text{(eq. A1)}$$

where *A*, *B*, and *C* are experimentally determined fractionation factors for oxygen isotope exchange between the two minerals (e.g., Chacko et al., 2001; Vho et al., 2020). In the FGB program, all fractionations (Δ's) are referenced to a common phase, usually quartz when present. Oxygen diffusivities for each mineral are calculated by the Arrhenius relation

$$D_i(T) = D_{0,i}e^{-\left(\frac{Q}{RT}\right)}, \quad \text{(eq. A2)}$$

where the preexponential factors, D_0 (m^2/s), and activation energies, Q (J/mol), for each phase are experimentally determined (e.g., Cole et al., 2001; Farver, 2010). The program then solves for concentration profiles (c_i, concentration as a function of distance from core to rim of a mineral grain) in each mineral using a one-dimensional Crank-Nicholson finite difference scheme with spherical or cylindrical geometry in the matrix form

$$\begin{bmatrix} 1 & & & & & & \\ -\kappa & 1+2\kappa & -\kappa & & & & \\ & -\kappa & 1+2\kappa & -\kappa & & & \\ & & \ddots & \ddots & \ddots & & \\ & & & -\kappa & 1+2\kappa & -\kappa & \\ & & & & & 1 & \end{bmatrix} \begin{bmatrix} c_{i,1}^{k+1} \\ c_{i,2}^{k+1} \\ c_{i,3}^{k+1} \\ \vdots \\ c_{i,n-1}^{k+1} \\ c_{i,n}^{k+1} \end{bmatrix} = \begin{bmatrix} grain\ boundary\ value \\ \kappa c_{i,1}^{k} + (1-2\kappa)c_{i,2}^{k} + \kappa c_{i,3}^{k} \\ \kappa c_{i,2}^{k} + (1-2\kappa)c_{i,3}^{k} + \kappa c_{i,4}^{k} \\ \vdots \\ \kappa c_{i,n-2}^{k} + (1-2\kappa)c_{i,n-1}^{k} + \kappa c_{i,n}^{k} \\ grain\ boundary\ value \end{bmatrix}$$

(eq. A3)

where $\kappa = D\Delta t/2(\Delta x)^2$, a factor that that must be less than ½ to prevent spurious oscillations; $c_{i,j}^{k}$ is the concentration ($\delta^{18}O$) at the j^{th} node in the mineral *i* at the k^{th} time step; and "*grain boundary value*" is the flux-modulated equilibrium grain boundary $\delta^{18}O$ value determined by solving equation A7 in the previous time step (Fig. 4B). Spatial steps in the finite difference grid in each mineral are ~0.5-20 μm. Time steps are small compared to the total model run duration (typically in the range 1,000 – 10,000 yrs), resulting in values of κ much less than ½.

The $\delta^{18}O$ flux is calculated for a given time step for a given mineral with a discretized version of Fick's first law:

$$J_i = -D_i \frac{\Delta c_i}{\Delta x_i} = D_i \frac{c_{n-1,j} - c_{n,j}}{\Delta x_i} \quad \text{(eq. A4)}$$

where the concentration difference is the $\delta^{18}O$ difference between the grain boundary node and first interior node of the mineral (Fig. 4A). Mass balance is then imposed on the system by requiring that all fluxes from all minerals sum to zero for a given time step:

$$\sum_{i=1}^{m} \chi_i A_i \nu_i J_i = 0 \quad \text{(eq. A5)}$$

Flux for each mineral *i* is weighted by the product of the mineral volume fraction in the rock, χ_i, the surface area of the mineral, A_i, and the oxygen density in the mineral, ν_i. The equilibrium fractionation equations (eq. A1) provide *m*-1 constraints for calculating the equilibrium oxygen isotope concentrations for a set of *m* minerals at a given temperature. The final m^{th} constraint is provided when the mass/flux balance constraint above is formulated as:

$$\sum_{i=1}^{m} \chi_i A_i \nu_i \left(\frac{D_i}{\Delta x_i} c_{i,n-1}\right) = \sum_{i=1}^{m} \chi_i A_i \nu_i \left(\frac{D_i}{\Delta x_i} c_{i,n}\right) \quad \text{(eq. A6)}$$

Then all fractionation and flux equations are solved simultaneously for updated equilibrium grain boundary $\delta^{18}O$ values:

$$\begin{bmatrix} 1 & -1 & 0 & \dots & 0 \\ 1 & 0 & -1 & \dots & 0 \\ \vdots & & & & \vdots \\ 1 & & & & -1 \\ k_1 & k_2 & \dots & \dots & k_m \end{bmatrix} \begin{bmatrix} c_{1,n}^{(k+1)} \\ c_{2,n}^{(k+1)} \\ \vdots \\ c_{m-1,n}^{(k+1)} \\ c_{m,n}^{(k+1)} \end{bmatrix} = \begin{bmatrix} \Delta_{1-2} \\ \Delta_{1-3} \\ \vdots \\ \Delta_{1-m} \\ \sum_{i=1}^{m} k_j c_{1,n-1}^{(k)} \end{bmatrix}. \quad \text{(eq. A7)}$$

Calculations in equations A1 through A7 occur for each time step after model initialization so that grain-boundary equilibrium fractionations, mineral $\delta^{18}O$ zoning profiles, and flux balance are updated on the same timescale.

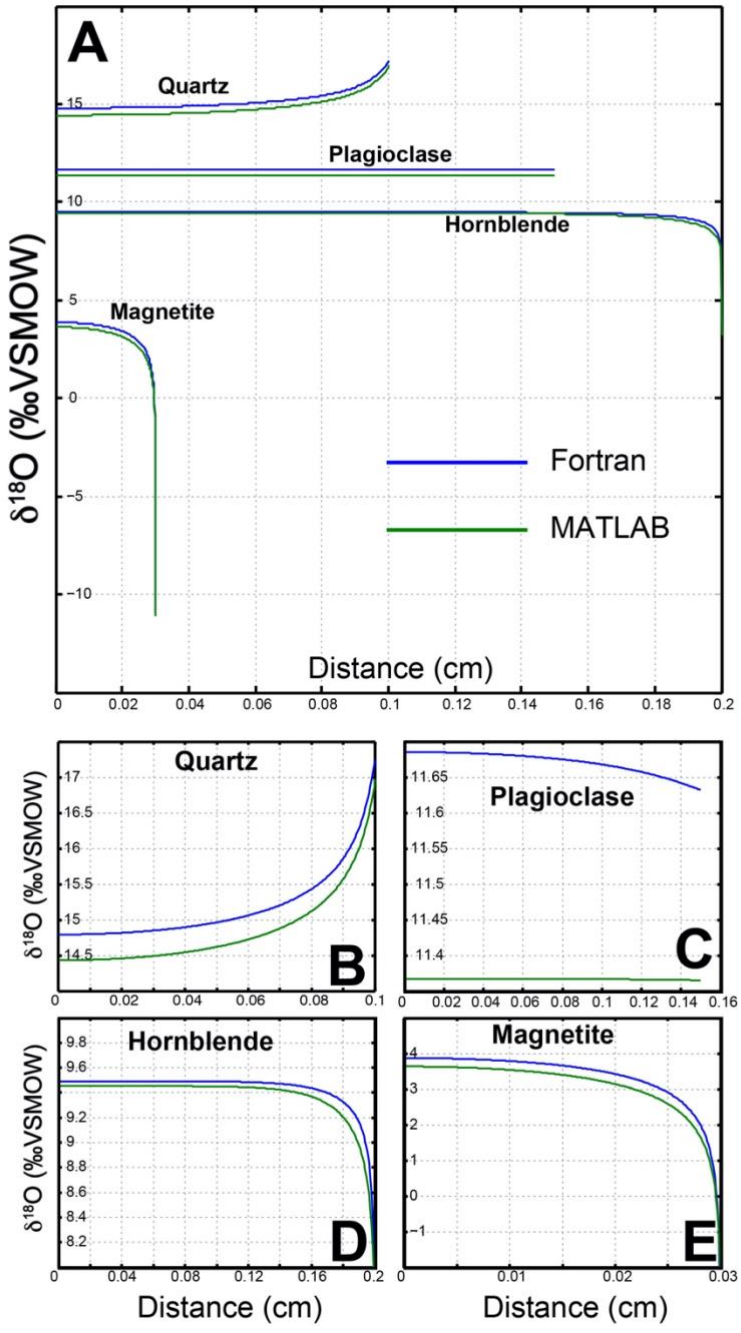

Figure S1: Graphical comparison of FGB model results with the original Fortran code (Eiler et al., 1994) versus the MATLAB code (Bonamici, 2013), which is the basis of the Python/C code of this study. Example is a hypothetical amphibolite rock composition at the end of a 45 m.y. model run with a T-1/t linear cooling history. (A) All mineral profiles at the same scale. (B)-(E) Mineral profiles at different, expanded scales showing the details of the model fits.

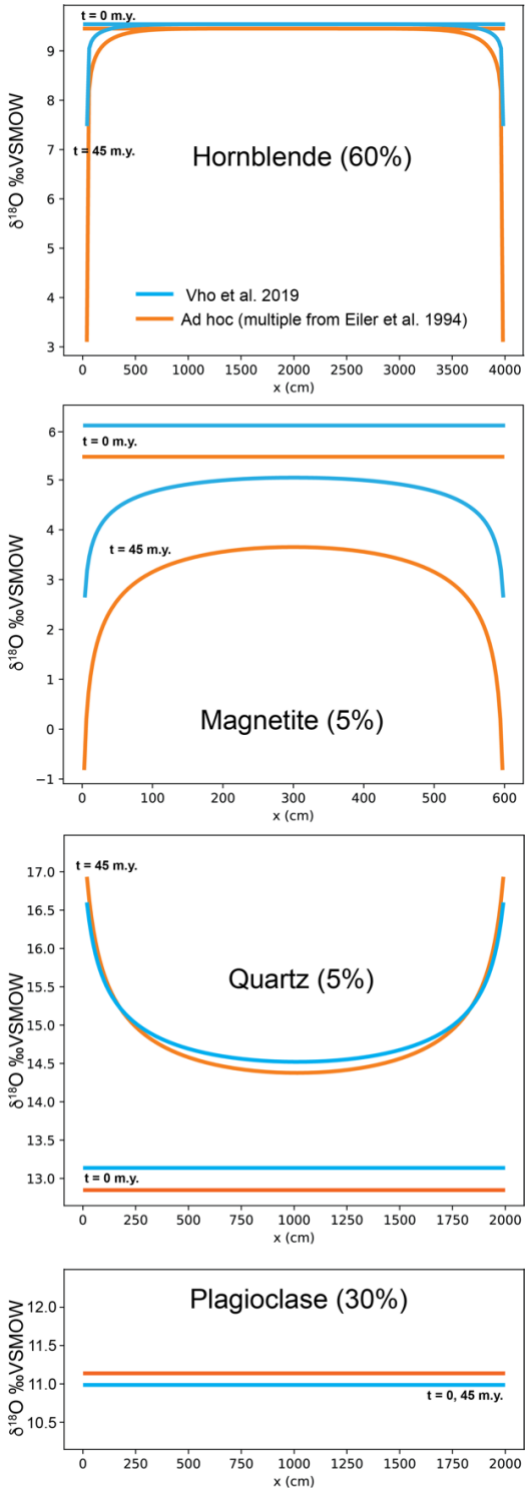

Figure S2: Graphical comparison of FGB forward models for a hypothetical amphibolite using ad hoc $\delta^{18}O$ fractionation factors (orange curves) and Vho et al.'s (2019) database of recalculated, internally consistent fractionation factors (blue curves). Modal percentages for each phase indicated next to the mineral label. Differences in predicted $\delta^{18}O$ would be indistinguishable by SIMS at current precision for all phases except magnetite.

B. Inverse approach – the Levenberg-Marquardt algorithm

Assuming a forward model, *G,* that accepts a vector of model inputs, ***m***, and produces a vector of data outputs, ***d***, the inverse problem, of finding model inputs given data outputs, can be expressed as the optimization problem (Aster et al., 2018):

$$min \sum_{i=1}^{n} \left(\frac{G(m_i)-d_i}{\sigma_i}\right)^2 \qquad \text{(eq. B1)}$$

In the general case, *G* is non-linear and its inverse may have many solutions. To prevent the overfitting of noise in data, a regularization term is added to the optimization problem:

$$min \sum_{i=1}^{n} \left(\frac{G(m_i)-d_i}{\sigma_i}\right)^2 + \beta \sum_{i=1}^{m} (Lm)_i^2 \qquad \text{(eq. B2)}$$

To select the optimal smoothing parameter, β , that balances data fit and model smoothness, L-curves are computed by running the inverse solver with progressively larger values of β, plotting the error $\|G(\boldsymbol{m}) - d\|^2$ versus the solution smoothness $\|L\boldsymbol{m}\|^2$, and selecting the β value at the kink of the L-curve (Fig. S1).

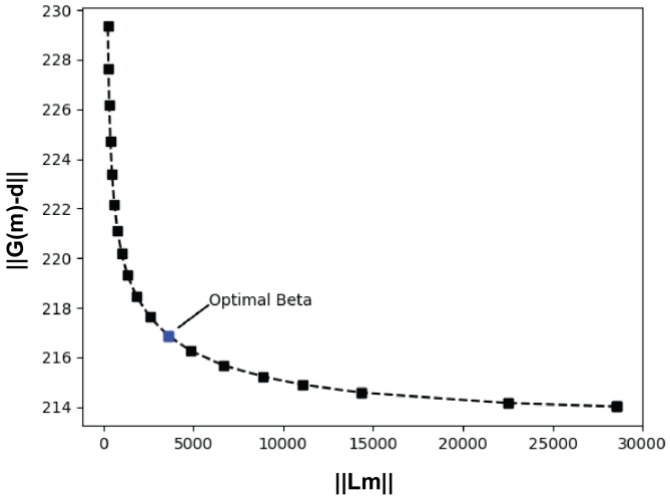

Figure S3: Example of L-curve used to choose optimal smoothing parameter.

The roughening matrix, *L*, can be constructed to penalize first or second order derivatives of the model vector ***m***. We apply us the second-order Tikhonov regularization approach where *L***m** is proportional to the second derivative of **m** and the roughening matrix is:

$$L = \begin{bmatrix} 1 & -2 & 1 & & & & \\ & 1 & -2 & 1 & & & \\ & & \ddots & \ddots & \ddots & & \\ & & & 1 & -2 & 1 & \\ & & & & 1 & -2 & 1 \end{bmatrix} \qquad \text{(matrix 1)}$$

This regularization approach has the added benefit of collapsing many possible solutions of the inverse problem to a single best solution when the data do not entirely constrain the model (Aster et al., 2018).

In the absence of an analytical solution for the general inverse optimization problem (nonlinear G), we use the iterative Levenberg-Marquardt (LM) algorithm. A vector valued function, F, is defined according to eq. 1 and 2, where σ_i represents the uncertainty in the data measurement d_i:

$$f_i = \frac{G(m)_i - d_i}{\sigma_i} \qquad \text{(eq. B3)}$$

$$F = \begin{bmatrix} f_1(m) \\ \vdots \\ f_n(m) \\ (Lm)_1 \\ \vdots \\ (Lm)_m \end{bmatrix} \qquad \text{(eq. B4)}$$

The LM algorithm starts with an initial solution and iteratively updates this solution by solving eq. 5 for $\Delta\boldsymbol{m}$, and then adding $\Delta\boldsymbol{m}$ to the current solution:

$$\left(\boldsymbol{J}\left(\boldsymbol{m}^{(k)}\right)^T \boldsymbol{J}\left(\boldsymbol{m}^{(k)}\right) + \beta^2 L^T L + \lambda I\right) \Delta\boldsymbol{m} = -\boldsymbol{J}\left(\boldsymbol{m}^{(k)}\right)^T \left(G\left(\boldsymbol{m}^{(k)}\right) - d\right) - \beta^2 L^T L \boldsymbol{m}^{(k)}, \quad \text{(eq. B5)}$$

where

$$\boldsymbol{m}^{(k+1)} = \boldsymbol{m}^{(k)} + \Delta\boldsymbol{m} \qquad \text{(eq. B6)}$$

$\boldsymbol{J}$ is the Jacobian of F. The parameter β is a tuning parameter that controls the inverse solver's priority for model smoothness. The parameter λ ensures convergence and is updated at each iteration depending on whether or not the solution is getting better. The LM algorithm has the advantage of converging where gradient descent method would but also has quadratic convergence under appropriate assumptions (Aster et al., 2018).

C. Applying the Levenberg-Marquardt Algorithm in Python and C

With the user setting model parameters related to rock mineralogy and texture and equilibrium fractionation factors and diffusivity parameters drawn from experimental databases, the FGB inverse solver attempts to recover the time-temperature history of a rock sample from the oxygen isotope diffusion profiles within grains from the sample. Because the LM algorithm is an iterative method, it requires an initial solution, and thus the first step is to propose and discretize a time-temperature history (Fig. S2). The actual input is a vector of temperatures, ***m***, corresponding to the temperature at each of the equally spaced time-periods. A linear interpolator is then used to create a continuous time-temperature history.

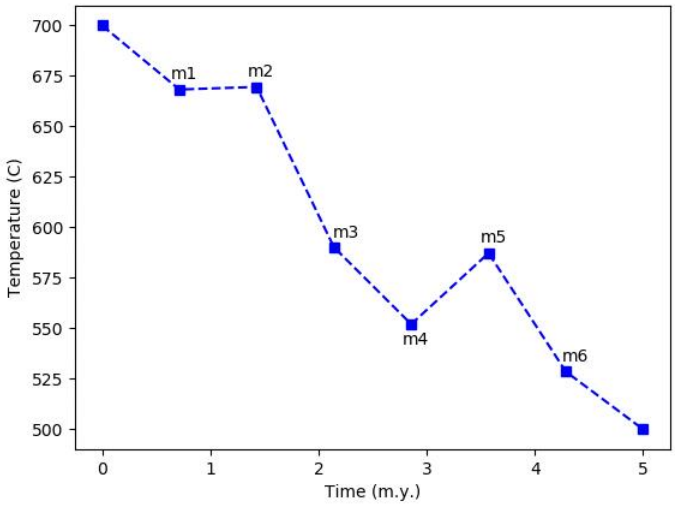

Figure S4: Example of the discretized model input.

The actual solution is assumed to be a linear interpolator between a finite number of points equally spaced apart. The user provides the initial guess T–t history in the form of a csv file formatted with times in the first column and corresponding temperatures in the second column. The LM algorithm is then applied with the vector of temperatures as the model input vector ***m***. At each model iteration, the temperature values in the second column are are updated by solving equation 5. If the error improves during an iteration, λ is multiplied by a factor of 1/8. Otherwise, it is doubled. The λ term is used to ensure convergence when the condition numbers of the matrices become large, as is often the case with quadratic methods and poor initial guesses (Aster et al., 2018).

D. Generating synthetic data for testing inverse model

Before applying the inverse algorithm to real world data, it is evaluated on simulated data to determine what features it is capable of recovering. The overall process is to start with a known time-temperature history, run the forward model, keep only a sample of the data points from the output, add noise to these data points, and then run the inverse solver on this noisy data. The sample of forward output that is kept and fed into the inverse solver is shown in Figures S3 and S4. The level of noise is chosen to match the current analytical uncertainty of SIMS oxygen isotope measurements (±0.14‰ 1 SD). This has been done for several different simulated temperature-time histories discussed in this manuscript.

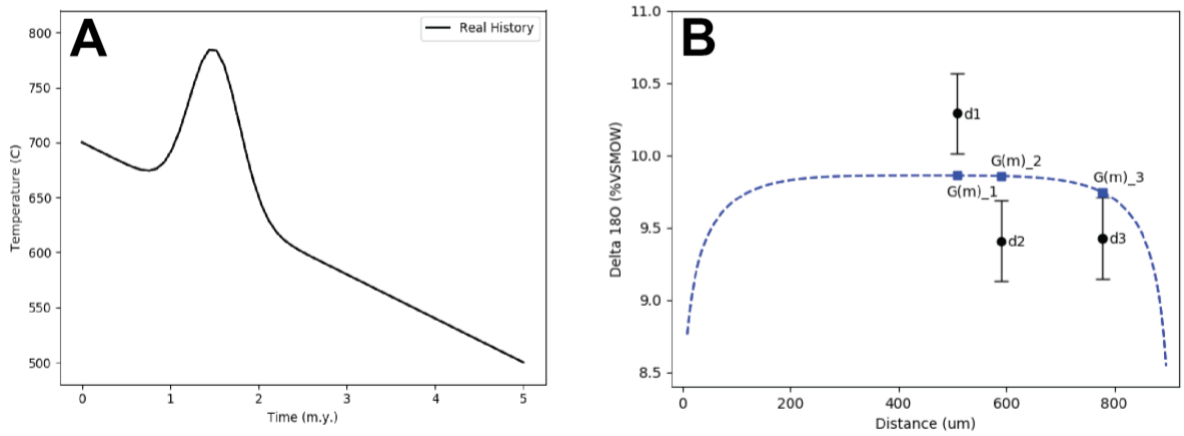

Figure S5: (A) Simulated temperature-time history with early heating spike superimposed on a linear cooling trend input into the FGB forward model. (B) Oxygen isotope zoning profile predicted by the FGB forward model for the mineral titanite in a simulated rock (blue dashed curve) and the sampling of data points from the zoning profile that are saved as input for inverse modeling (points). Points labeled $G(\boldsymbol{m})_i$ are the forward model output and points labeled d_i are the values that has been obscured with noise and then stored for inversion tests.

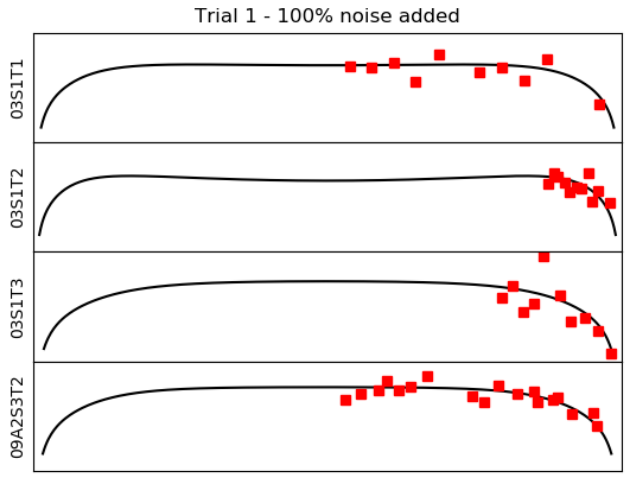

Figure S6: Examples of simulated datasets with different numbers and spatial distributions of isotope measurements that mimic real titanite datasets.

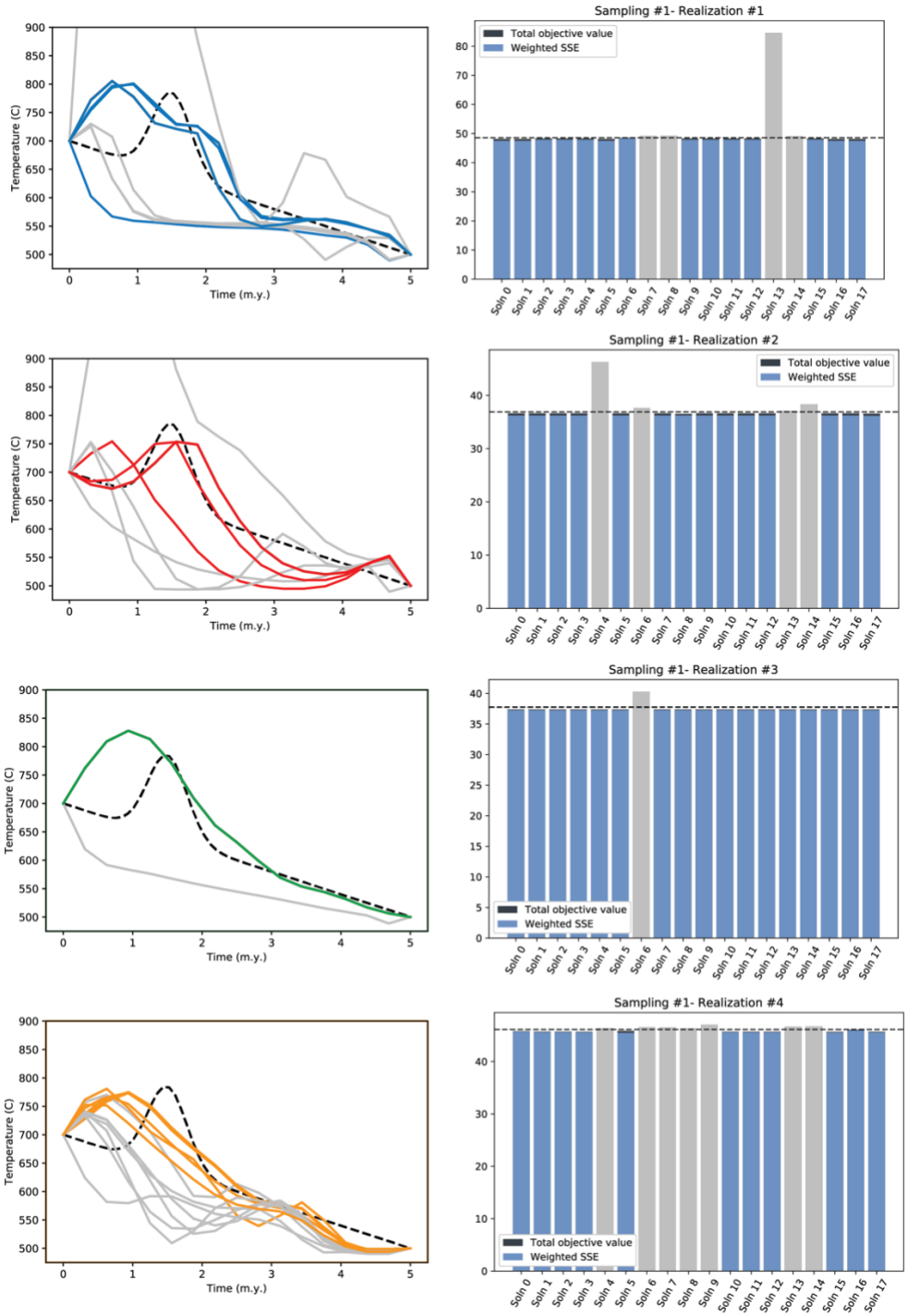

Figure S7: Inverse model solver results for sampling scheme 1, using four different noise realizations and 18 initial guess solutions for each realization. Lefthand column plots show T–t paths for acceptable solutions. Righthand column plots show total objective function values for each noise realization. Solutions with total objective values >1% above the lowest total objective value for the realization are rejected (gray bars to right, gray paths to left).

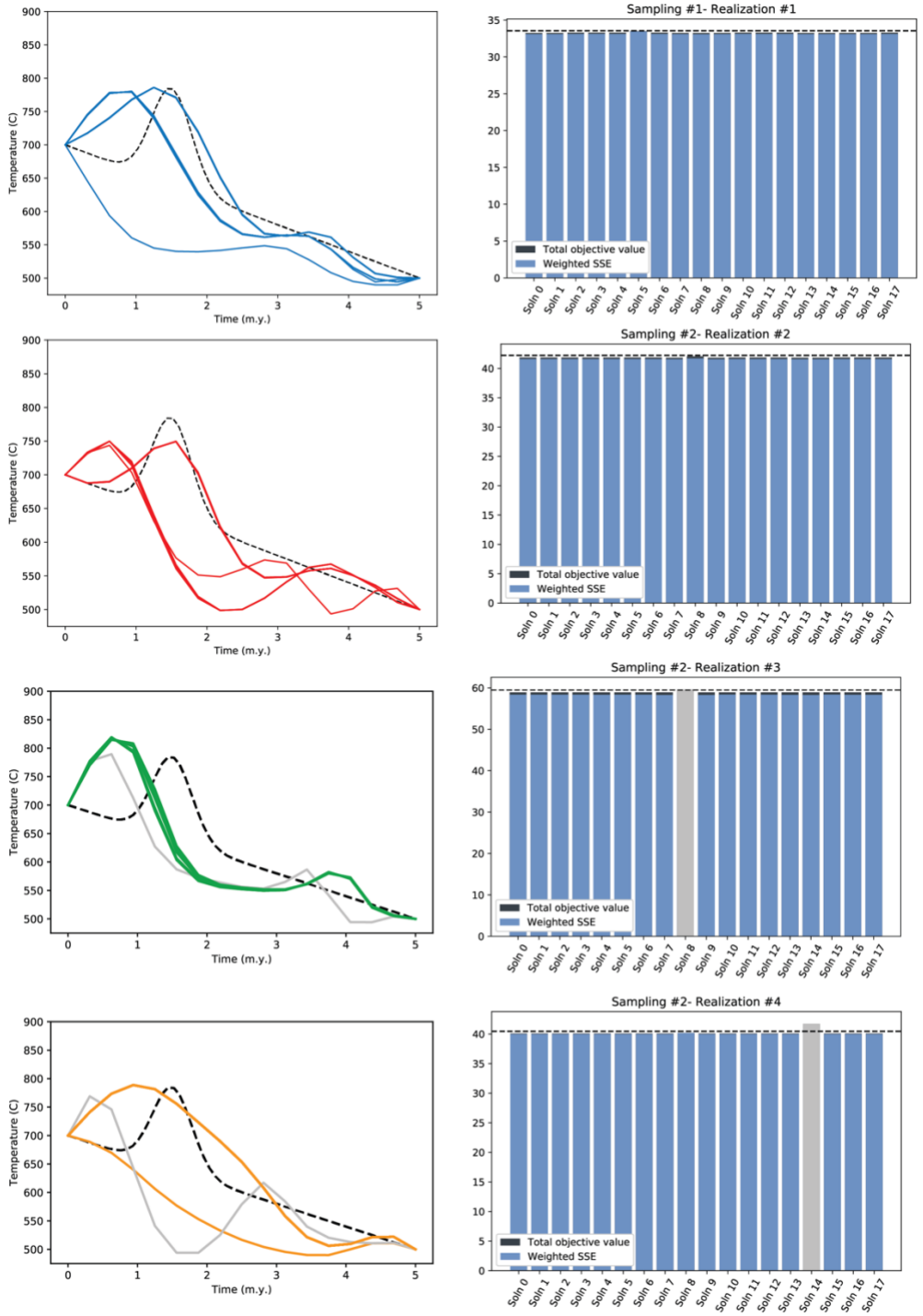

Figure S8: Inverse model solver results for sampling scheme 2, using four different noise realizations and 18 initial guess solutions for each realization. Lefthand column plots show T–t paths for acceptable solutions. Righthand column plots show total objective function values for each noise realization. Solutions with total objective values >1% above the lowest total objective value for the realization are rejected (gray bars to right, gray paths to left).

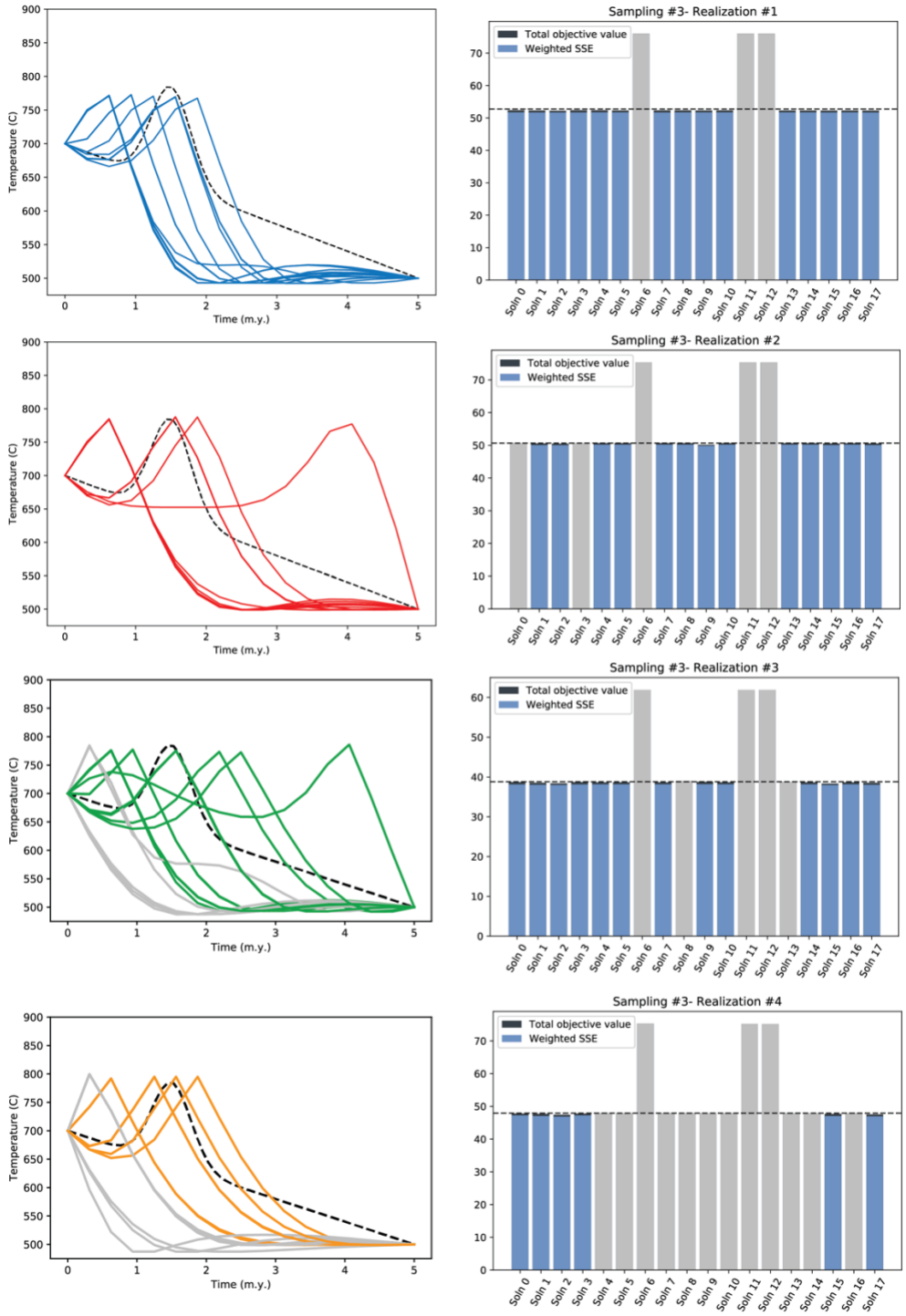

Figure S9: Inverse model solver results for sampling scheme 3, using four different noise realizations and 18 initial guess solutions for each realization. Lefthand column plots show *T*–*t* paths for acceptable solutions. Righthand column plots show total objective function values for each noise realization. Solutions with total objective values >1% above the lowest total objective value for the realization are rejected (gray bars to right, gray paths to left).

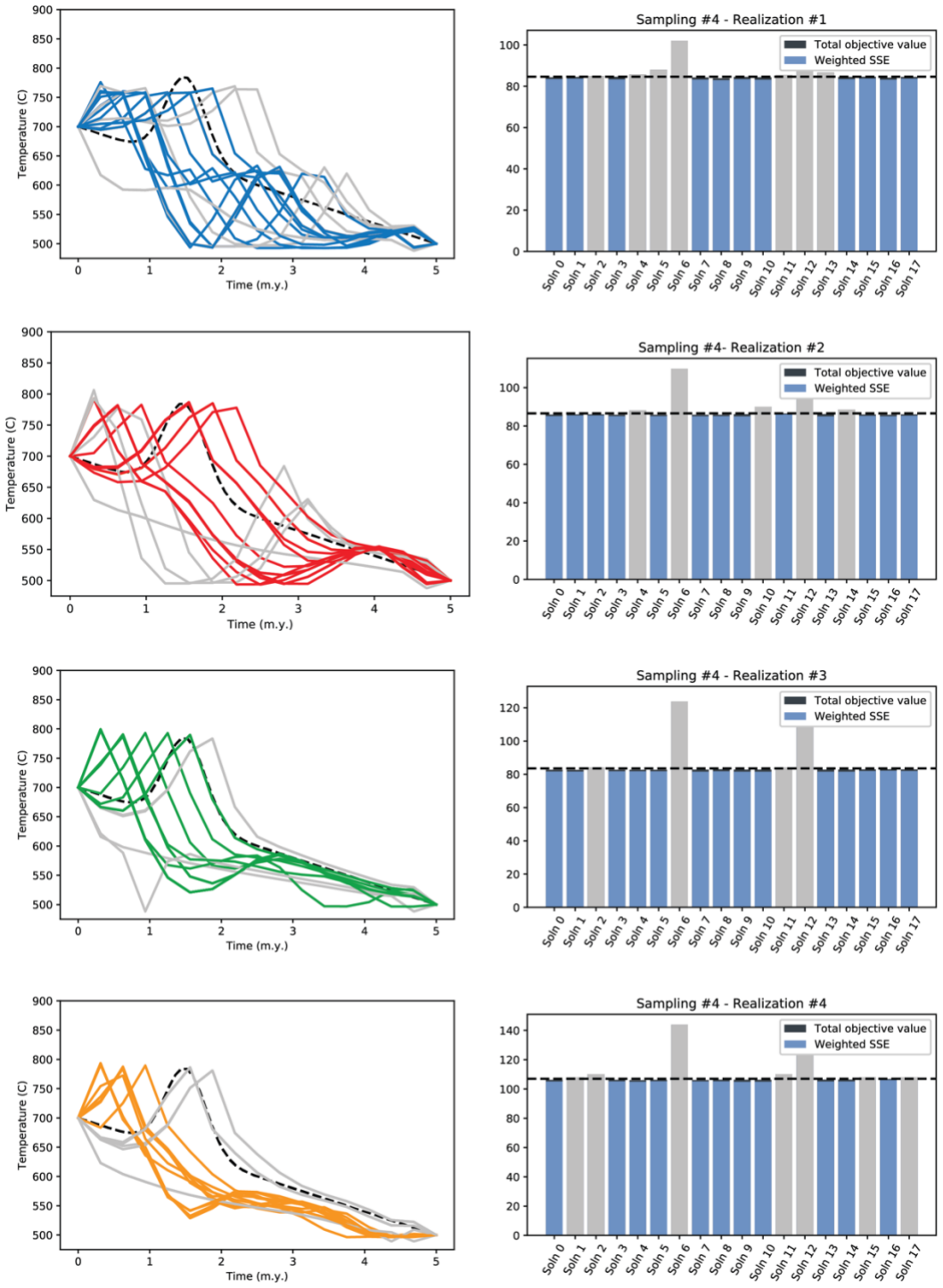

Figure S10: Inverse model solver results for sampling scheme 4, using four different noise realizations and 18 initial guess solutions for each realization. Lefthand column plots show T–t paths for acceptable solutions. Righthand column plots show total objective function values for each noise realization. Solutions with total objective values >1% above the lowest total objective value for the realization are rejected (gray bars to right, gray paths to left).

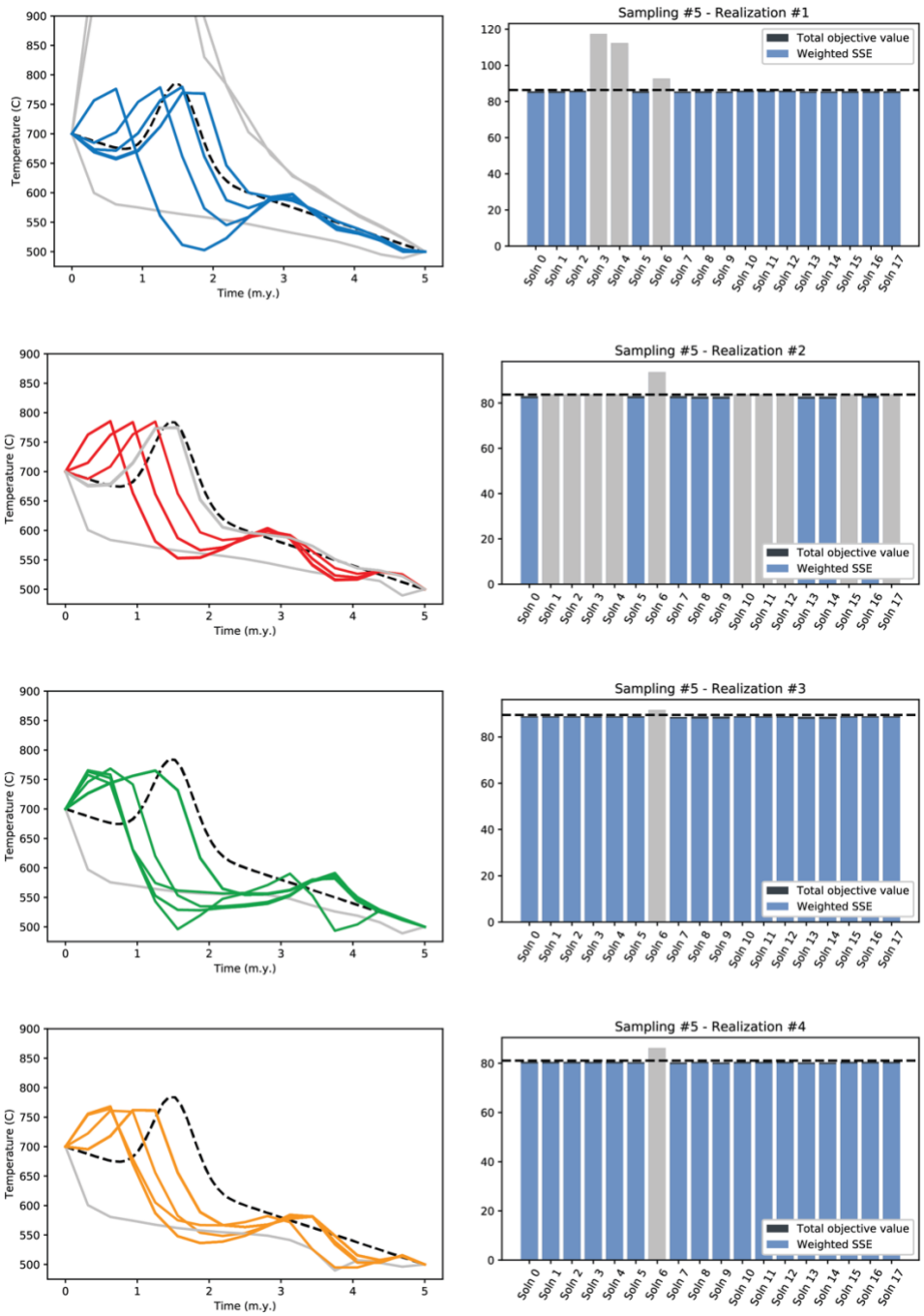

Figure S11: Inverse model solver results for sampling scheme 5, using four different noise realizations and 18 initial guess solutions for each realization. Lefthand column plots show T–t paths for acceptable solutions. Righthand column plots show total objective function values for each noise realization. Solutions with total objective values >1% above the lowest total objective value for the realization are rejected (gray bars to right, gray paths to left).

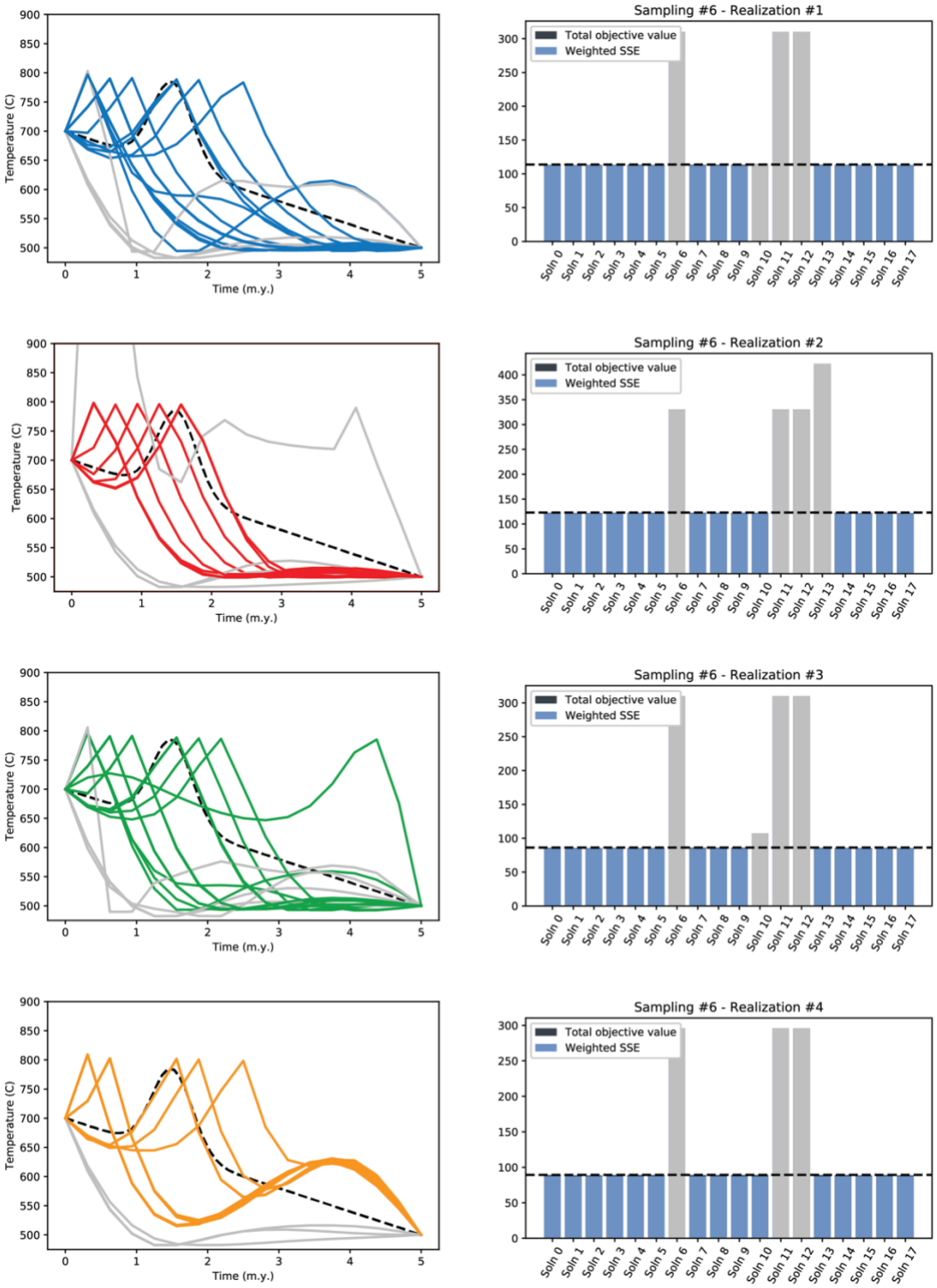

Figure S12: Inverse model solver results for sampling scheme 6, using four different noise realizations and 18 initial guess solutions for each realization. Lefthand column plots show *T*–*t* paths for acceptable solutions. Righthand column plots show total objective function values for each noise realization. Solutions with total objective values >1% above the lowest total objective value for the realization are rejected (gray bars to right, gray paths to left).

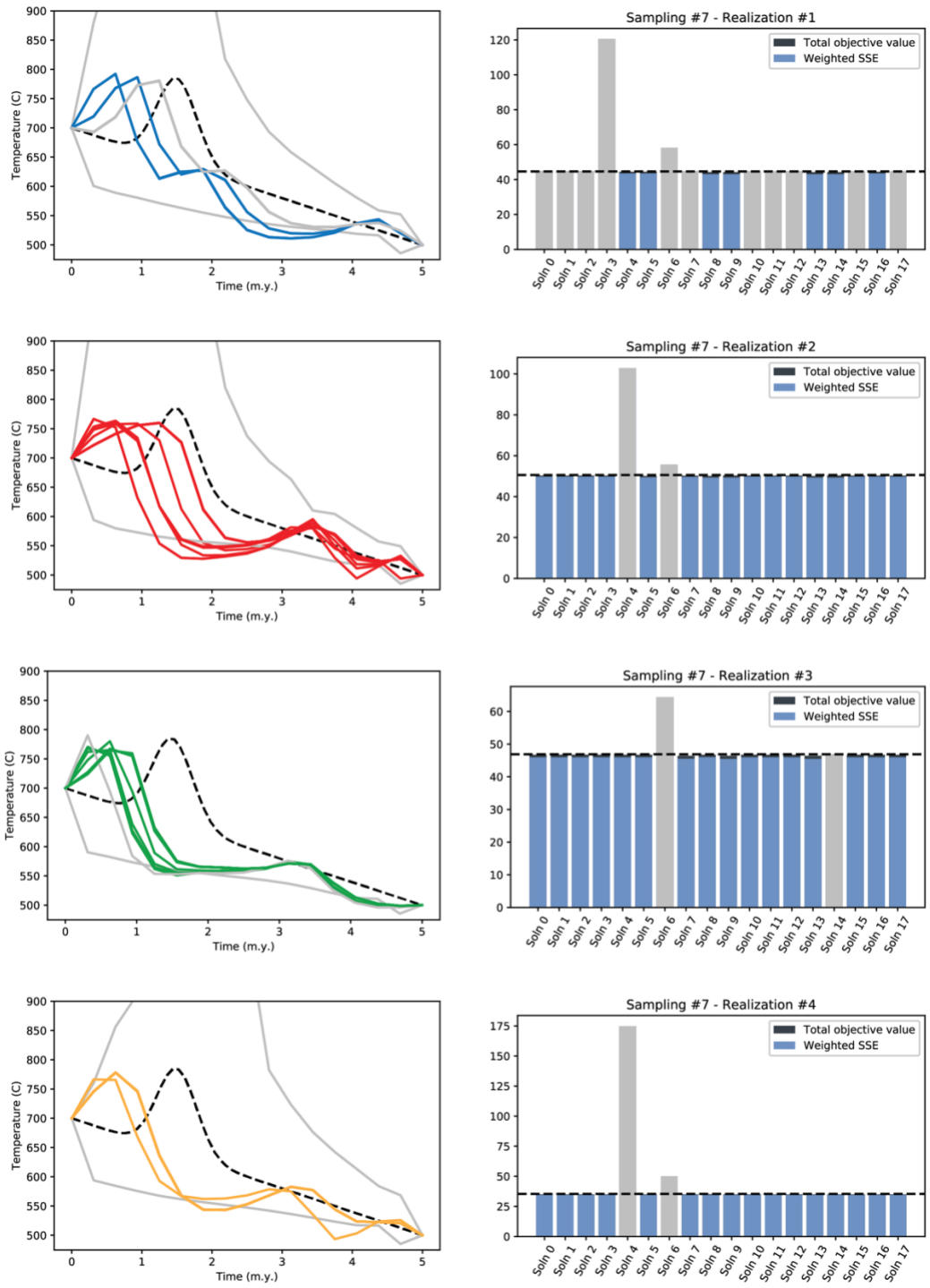

Figure S13: Inverse model solver results for sampling scheme 7, using four different noise realizations and 18 initial guess solutions for each realization. Lefthand column plots show *T*–*t* paths for acceptable solutions. Righthand column plots show total objective function values for each noise realization. Solutions with total objective values >1% above the lowest total objective value for the realization are rejected (gray bars to right, gray paths to left).

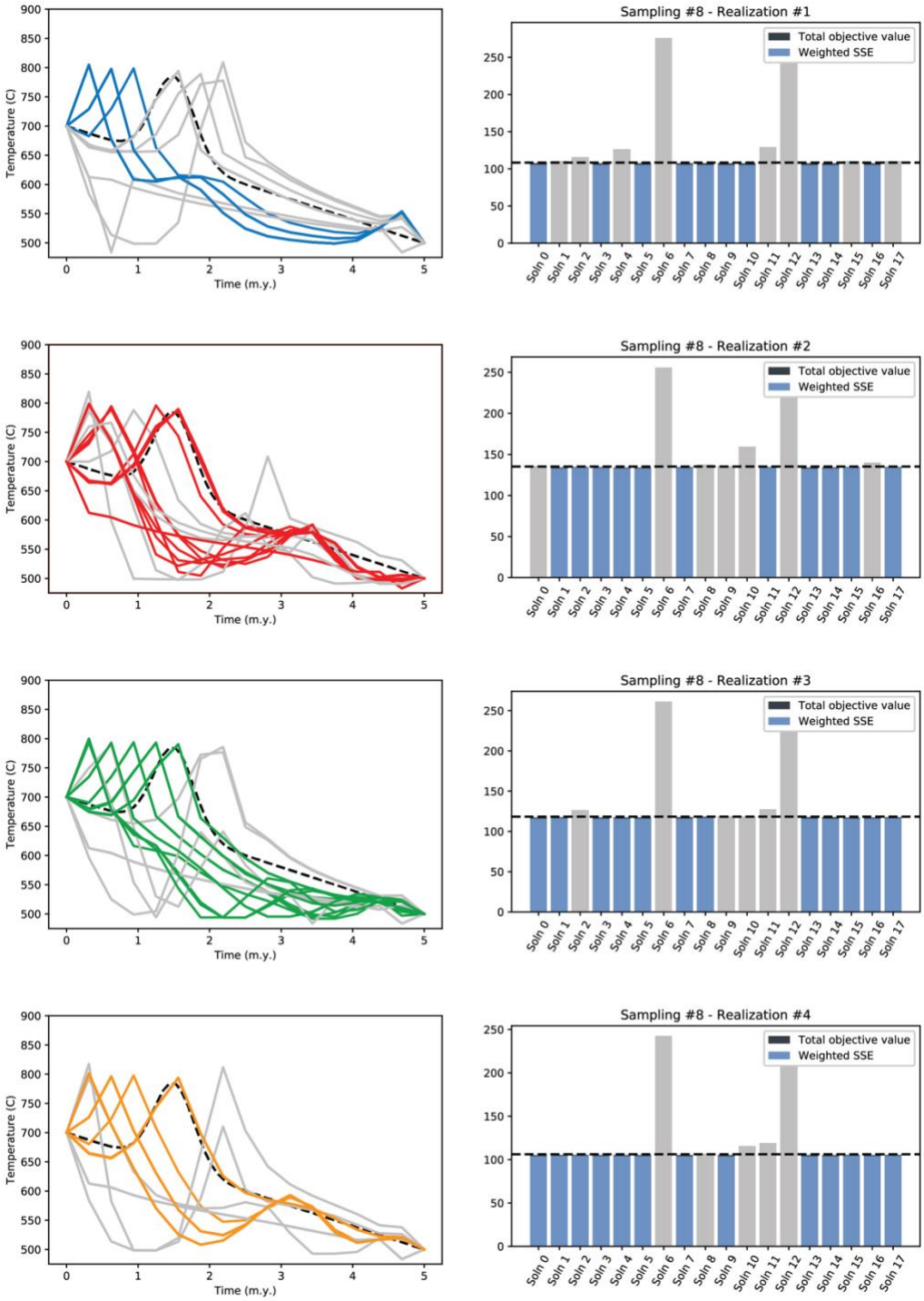

Figure S14: Inverse model solver results for sampling scheme 8, using four different noise realizations and 18 initial guess solutions for each realization. Lefthand column plots show T–t paths for acceptable solutions. Righthand column plots show total objective function values for each noise realization. Solutions with total objective values >1% above the lowest total objective value for the realization are rejected (gray bars to right, gray paths to left).